# Triaxial angular momentum projection and configuration mixing calculations with the Gogny force

Tomás R. Rodríguez* and J. Luis Egido
*Departamento de Física Teórica, Universidad Autónoma de Madrid, E-28049 Madrid, Spain*
(Received 15 April 2010; published 25 June 2010)

We present the first implementation in the $(\beta, \gamma)$ plane of the generator coordinate method with full triaxial angular momentum and particle number projected wave functions using the Gogny force. Technical details about the performance of the method and the convergence of the results in both the symmetry restoration and the configuration mixing parts are discussed in detail. We apply the method to the study of $^{24}$Mg; the calculated energies of excited states as well as the transition probabilities are compared to the available experimental data, showing a good overall agreement. In addition, we present the RVAMPIR approach, which provides a good description of the ground and $\gamma$ bands in the absence of strong mixing.

DOI: 10.1103/PhysRevC.81.064323 PACS number(s): 21.60.Jz, 21.10.Re, 21.60.Ev, 27.30.+t

## I. INTRODUCTION

Self-consistent mean-field methods with effective phenomenological interactions and their extensions beyond the mean field provide the appropriate theoretical tools for describing many phenomena along the whole chart of nuclides, from light to medium, to heavy, and to superheavy nuclei in or far away from the stability valley [1]. On the one hand, the success of these methods is related to the high quality of the phenomenological effective interactions used: Skyrme, Gogny, or relativistic mean field (RMF). On the other hand, the mean-field method allows the inclusion of many correlations within a very simple intrinsic product wave function. Hence, bulk properties such as masses and radii are very well described at the mean-field level. However, in some cases this picture fails to take into account important correlations, and methods beyond the mean-field approach have to be applied. Furthermore, because the mean field is defined in the intrinsic frame it is mandatory to go beyond this approximation to evaluate excitation energies or transition probabilities in the laboratory system.

There are several methods to incorporate the correlations missing at the mean-field level. Normally, the intrinsic wave functions are allowed to break relevant symmetries of the system, for example, particle number, rotational and translational invariance, parity, and time-reversal, to enlarge the variational space and incorporate, for instance, deformation or superfluidity in the mean-field picture. This leads to a degeneracy of the wave functions rotated in the gauge space associated with the broken symmetry. An appropriate superposition of these wave functions provides a symmetry conserving many-body wave function and an additional lowering of the energy of the system. In this way, using projection techniques [2], many correlations are obtained by restoring some or all of these symmetries. Furthermore, the mixing of different mean-field configurations within the general framework of the generator coordinate method (GCM) [2] allows the inclusion of quantum fluctuations along some relevant collective variables such as the multipole moments.

Most of the currently used beyond-mean-field calculations with effective forces include two symmetry restorations, that is, particle number (PN) and angular momentum projection (AMP) and configuration mixing along the axial quadrupole deformation [1,3,4]. This approach (axial GCM-PNAMP) has been successfully applied to study many phenomena such as, for example, the appearance or degradation of shell closures in neutron-rich nuclei [3,5–7], shape coexistence in proton-rich Kr [8] or Pb [9,10] isotopes, or shape transitions in the $A \sim 150$ region [11,12]. However, the intrinsic wave functions used there were restricted to have axial symmetry, with $K = 0$, because this assumption simplifies considerably the angular momentum projection and lightens the computational burden significantly. This restriction is one of the major drawbacks of the method because it limits its applicability to systems where triaxiality does not play an important role. However, many exciting experimental and theoretical phenomena are closely related to the triaxial degree of freedom, including, for instance, the presence of $\gamma$ bands in the low-lying energy spectra and $\gamma$ softness, shape coexistence, and shape transitions in transitional regions [13–20]; the lowering of fission barriers along the triaxial path [21–23]; the influence of triaxial deformation in the ground state for the mass models [24,25]; triaxiality at high spin [26–28]; the observation of $K$ bands and isomeric states in the Os region [29–31]; or some other exotic excitation modes such as wobbling motion and chiral bands [32–34].

From the theoretical point of view some approaches beyond the mean field have been proposed to study the triaxial effects. In particular, one of the most widely used is the collective Hamiltonian [2] given in different versions depending on the underlying nucleon-nucleon interaction used to define the collective potential, namely pairing-plus-quadrupole [35], interacting boson model [36], Nilsson Woods-Saxon [26], Gogny [37–39], or RMF [40]. This model has been applied successfully to describe some of the experimental features just mentioned. However, the collective Hamiltonian can be understood as a Gaussian overlap approach (GOA) of the triaxial GCM and this description should be improved by including properly the effects of the symmetry

*Present address: GSI Helmholtzzentrum für Schwerionenforschung, D-64259 Darmstadt, Germany.

 

restoration and the full configuration mixing without any GOA approximation.

In the past, exact angular momentum projection with triaxial intrinsic wave functions without GCM has been carried out only for schematic forces and/or reduced configuration spaces. Examples are the projection of BCS [41] or cranked Hartree-Fock-Bogoliubov (CHFB) states [42] with the pairing-plus-quadrupole interaction, the projection of cranked Hartree-Fock (CHF) states (no pairing) with schematic [43] and full Skyrme interactions [44], or angular momentum projection before variation with particle number and parity restoration in limited shell-model spaces [45,46].

However, recent improvement in computational capabilities enabled the first implementations of the angular momentum projection of triaxial intrinsic wave functions in the whole $(\beta, \gamma)$ plane with effective forces. In particular, Bender and Heenen reported GCM calculations with particle number and triaxial angular momentum projection (PNAMP) with the Skyrme SLy4 interaction [47]. In this work, the intrinsic wave functions were found by solving the Lipkin-Nogami (LN) equations. Yao *et al.* presented the implementation of the triaxial angular momentum projection [48] and the extension to the GCM [49] for the RMF framework. In the latter work no particle number projection has been performed and the mean-field states are found by solving the RMF + BCS instead of the full HFB or LN equations. These approximations could lead to a poor description of important pairing correlations, especially in the weak-pairing regime where even spurious phase transitions appear [3,50].

In this paper we present the first implementation of the generator coordinate method with particle number and angular momentum projected (GCM-PNAMP) triaxial HFB wave functions with the finite-range density-dependent Gogny force [51]. The finite range of the Gogny force provides excellent pairing properties and is often used as a benchmark in this respect. Furthermore it is able to provide at the same time both good global as well as spectroscopic properties [52,53]. The intrinsic HFB states are found by solving the variation after particle number projection (VAP-PN) equations [54]. This fact constitutes the main methodological difference with respect to the calculations reported in Ref. [47]. This is a very important difference because VAP-PN allows the inclusion of the pairing correlations in a very efficient way, yielding a significant improvement of the final results with respect to other approaches [3,54].

In nuclei without strong mixing the variation after mean-field projection in realistic model spaces (VAMPIR) [45] approach has been very successful. In this approach only one HFB wave function is considered, which is determined by minimization of the projected energy (i.e. the VAP approach for both the AM and the PN projections). A full VAMPIR approach with the Gogny force and large configuration spaces is not yet feasible. Instead we use an approximation to it, called RVAMPIR, which, as we shall see in the case nucleus studied in this article, provides very reasonable results for the ground and $\gamma$ bands with much less effort than in the GCM approach.

The paper is organized as follows. In Sec. II we will give an overview of the theoretical framework. Then, we will focus our analysis on the nucleus $^{24}$Mg, which has been studied as a test case in earlier implementations of the GCM-PNAMP method with Skyrme and relativistic interactions. In particular, in Sec. III we will show a standard axially symmetric calculation that allows us to make an educated guess for some relevant parameters needed in the full calculation such as the number of major oscillator shells or the relevant deformations ranges. In Sec. IV we will analyze in detail the simpler PNAMP method, studying the convergence of the integrals in the Euler angles, giving some consistency requirements, and showing the role of having an adequate mesh in the $(\beta, \gamma)$ plane. In Sec. V we will show the final results for the calculated spectrum and $B(E2)$ transition strengths of $^{24}$Mg and give comparison with experimental data. Finally, a brief summary and outlook on future work will be addressed in Sec. VI.

## II. THEORETICAL FRAMEWORK

### A. Generator coordinate method with particle number and angular momentum projected states

In the present approach, the final many-body wave functions that describe the different states of an even-even nucleus with $Z(N)$ number of protons (neutrons) are written as

$$|IM;NZ\sigma\rangle = \sum_{K\beta\gamma} f^{I;NZ,\sigma}_{K\beta\gamma} |IMK;NZ;\beta\gamma\rangle, \tag{1}$$

where $(\beta, \gamma)$ are quadrupole deformation parameters (see the following), $\sigma = 1, 2, \ldots$ labels the levels for a given value of the angular momentum $I$ and $M, K$ are the projections of $\vec{I}$ on the laboratory and intrinsic $z$ axes, respectively. The coefficients $f^{I;NZ,\sigma}_{K\beta\gamma}$ of the linear combination are found by minimizing the energy within the nonorthogonal set of wave functions $\{|IMK;NZ;\beta\gamma\rangle\}$. These states are obtained by projecting the intrinsic mean-field states $|\Phi(\beta,\gamma)\rangle$ onto good particle number and angular momentum:

$$|IMK;NZ;\beta\gamma\rangle = \frac{2I+1}{8\pi^2} \int \mathcal{D}^{I*}_{MK}(\Omega) \hat{R}(\Omega) \hat{P}^N \hat{P}^Z |\Phi(\beta,\gamma)\rangle d\Omega, \tag{2}$$

with $\hat{P}^N = \frac{1}{2\pi}\int_0^{2\pi} e^{i\varphi(\hat{N}-N)} d\varphi$ the neutron number projector (where $\varphi$ is the associated gauge angle) and $\hat{P}^Z$ the proton number projector, and with $\hat{R}(\Omega)$ and $\mathcal{D}^{I*}_{MK}(\Omega)$ the rotation operator and the Wigner matrices [55] in the Euler angles $\Omega = (a, b, c)$,[1] respectively. In principle, the ranges for these angles are $(0 \leqslant a \leqslant 2\pi, 0 \leqslant b \leqslant \pi, 0 \leqslant c \leqslant 2\pi)$. However, for intrinsic HFB states $[|\Phi(\beta,\gamma)\rangle]$, which are symmetric under time reversal and simplex symmetries, the intervals for both gauge and Euler angles can be reduced to $(0 \leqslant \varphi \leqslant \pi/2)$ and $(0 \leqslant a \leqslant \pi/2, 0 \leqslant b \leqslant \pi/2, 0 \leqslant c \leqslant \pi)$, respectively [47].

The wave functions [Eq. (2)] are eigenstates of the particle number and angular momentum operators:

$$\hat{N}|IMK;NZ;\beta\gamma\rangle = N|IMK;NZ;\beta\gamma\rangle, \tag{3}$$

$$\hat{Z}|IMK;NZ;\beta\gamma\rangle = Z|IMK;NZ;\beta\gamma\rangle, \tag{4}$$

[1] We choose for the Euler angles the notation $\Omega = (a, b, c)$ instead of the usual $(\alpha, \beta, \gamma)$ to avoid confusion with the deformation parameters $(\beta, \gamma)$.

$$\hat{I}^2|IMK;NZ;\beta\gamma\rangle = \hbar^2 I(I+1)|IMK;NZ;\beta\gamma\rangle, \quad (5)$$

$$\hat{I}_z|IMK;NZ;\beta\gamma\rangle = \hbar M|IMK;NZ;\beta\gamma\rangle, \quad (6)$$

$$\hat{I}_3|IMK;NZ;\beta\gamma\rangle = \hbar K|IMK;NZ;\beta\gamma\rangle. \quad (7)$$

The intrinsic HFB states ($|\Phi(\beta,\gamma)\rangle$) are obtained by minimizing the particle number projected energy functional $E^{N,Z}[\bar{\Phi}(\beta,\gamma)]$ (VAP) [54]. This is one of the most relevant parts in the calculation because the quality of the result largely depends on the structure of the intrinsic HFB-type wave functions used. In contrast to other methods such as plain HFB or projected Lipkin-Nogami (PLN), the VAP-PN performs the restoration of the particle number symmetry in an optimal way, including pairing correlations in both the weak- and strong-pairing regimes [3]. This is especially relevant in GCM-like theories where a large grid of $(\beta,\gamma)$ points is needed. The strength of the pairing correlations has a strong dependence on the single-particle level density and the latter one itself with the deformation parameters. This implies that a strongly $(\beta,\gamma)$ dependent oscillating pairing regime appears in the calculations and consequently theories such as plain HFB (BCS) or PLN (LN) are unable to cope with this challenge of providing wave functions of oscillating goodness. Only a VAP-PN approach warrants high-quality solutions independently of the $(\beta,\gamma)$ values.

In dealing with effective forces such as Skyrme, relativistic, and Gogny, a natural separation of the interaction into the two-body Hamiltonian $\hat{H}_{2b}$ on the one hand and the density-dependent part, $\varepsilon^{N,Z}_{DD}[\Phi]$, on the other emerges. In our case, we are using the Gogny D1S interaction [51] and $\hat{H}_{2b}$ corresponds to the kinetic energy (the two-body part with the center-of-mass correction included) plus the spin-orbit, Coulomb, and the finite-range central potentials. In the calculations, all direct, exchange, and pairing terms are included [56]. The VAP-PN principle provides

$$\delta E^{N,Z}[\bar{\Phi}(\beta,\gamma)]|_{\bar{\Phi}=\Phi} = 0, \quad (8)$$

where

$$E^{N,Z}[\Phi] = \frac{\langle\Phi|\hat{H}_{2b}\hat{P}^N\hat{P}^Z|\Phi\rangle}{\langle\Phi|\hat{P}^N\hat{P}^Z|\Phi\rangle} + \varepsilon^{N,Z}_{DD}[\Phi] - \lambda_{q_{20}}\langle\Phi|\hat{Q}_{20}|\Phi\rangle - \lambda_{q_{22}}\langle\Phi|\hat{Q}_{22}|\Phi\rangle. \quad (9)$$

In a beyond-mean-field method, and in particular for the particle number projection, we need a reasonable prescription for the spatial density, which we shall call $\rho_{int}(\vec{r})$, that enters in $\varepsilon^{N,Z}_{DD}[\Phi]$, the density-dependent term of the interaction. In this work, assuming the phenomenological nature of these interactions and considering that the restoration of the particle number symmetry is performed not in the coordinate but in the gauge space, we have chosen the number projected spatial density prescription that has proven to be free of divergences [54] and to give very good results for describing many phenomena along the nuclear chart:

$$\rho^{NZ}_{int}(\vec{r}) \equiv \frac{\langle\Phi|\hat{\rho}(\vec{r})P^N P^Z|\Phi\rangle}{\langle\Phi|P^N P^Z|\Phi\rangle}, \quad (10)$$

with $\hat{\rho}(\vec{r}) \equiv \int d\vec{r}\,'\delta(\vec{r}-\vec{r}\,')$. As shown in Ref. [54] for the PNP and in Ref. [57] for the Lipkin-Nogami approach, the use of the projected density or the so-called mixed prescription (in the case when the latter is free of potential divergences) will give very similar results. Furthermore, we see in Eq. (9) that the minimization is performed under constraints on the quadrupole deformation operators $\hat{Q}_{2\mu}$. The Lagrange multipliers $\lambda_{q_{2\mu}}$ ensure that the following conditions are fulfilled in the intrinsic state:

$$\begin{aligned}\lambda_{q_{20}} &\rightarrow \langle\Phi|\hat{Q}_{20}|\Phi\rangle = q_{20},\\ \lambda_{q_{22}} &\rightarrow \langle\Phi|\hat{Q}_{22}|\Phi\rangle = q_{22}.\end{aligned} \quad (11)$$

In addition, the deformation parameters $(\beta,\gamma)$ are directly related to $(q_{20}, q_{22})$ by

$$q_{20} = \frac{\beta\cos\gamma}{C}, \quad q_{22} = \frac{\beta\sin\gamma}{\sqrt{2}C}, \quad C = \sqrt{\frac{5}{4\pi}}\frac{4\pi}{3r_0^2A^{5/3}}, \quad (12)$$

with $r_0 = 1.2$ fm and $A$ the mass number. These constraints allow us to explore the $(\beta,\gamma)$ plane to generate the wave functions to be used in the configuration mixing calculations.

We now describe the GCM to obtain the final spectrum ($E^{I;NZ;\sigma}$) and the coefficients $f^{I;NZ,\sigma}_{K\beta\gamma}$ given in Eq. (1). Minimization of the energy with respect to the coefficients $f^{I;NZ,\sigma}_{K\beta\gamma}$ leads to the Hill-Wheeler-Griffin (HWG) equation

$$\sum_{K'\beta'\gamma'}\left(\mathcal{H}^{I;NZ}_{K\beta\gamma K'\beta'\gamma'} - E^{I;NZ;\sigma}\mathcal{N}^{I;NZ}_{K\beta\gamma K'\beta'\gamma'}\right)f^{I;NZ;\sigma}_{K'\beta'\gamma'} = 0, \quad (13)$$

which has to be solved for each value of the angular momentum. The GCM norm and energy overlaps have been defined as

$$\begin{aligned}\mathcal{N}^{I;NZ}_{K\beta\gamma K'\beta'\gamma'} &\equiv \langle IMK;NZ;\beta\gamma|IMK';NZ;\beta'\gamma'\rangle,\\ \mathcal{H}^{I;NZ}_{K\beta\gamma K'\beta'\gamma'} &\equiv \langle IMK;NZ;\beta\gamma|\hat{H}_{2b}|IMK';NZ;\beta'\gamma'\rangle\\ &\quad + \varepsilon^{IKK';NZ}_{DD}[\Phi(\beta,\gamma),\Phi'(\beta',\gamma')].\end{aligned} \quad (14)$$

In the last expression, we have separated again the energy overlap into the contribution of the pure Hamiltonian part of the interaction and the density-dependent term. In the latter, we have used the particle number projected spatial density combined with the mixed prescription for the angular momentum projection and GCM part, namely,

$$\rho^{NZ}_{int}(\Omega,\vec{r}) \equiv \frac{\langle\Phi|\hat{\rho}(\vec{r})\hat{R}(\Omega)P^N P^Z|\Phi'\rangle}{\langle\Phi|\hat{R}(\Omega)P^N P^Z|\Phi'\rangle}. \quad (15)$$

This prescription is suitable for dealing with the restoration of broken symmetries in the coordinate space such as the rotational invariance or the spatial parity.

Once we have calculated the corresponding GCM overlaps, the next step consists in solving the HWG equations [Eq. (13)]. To cope with the problem of the linear dependence one first introduces a orthonormal basis defined by the eigenvalues $n^{I;NZ}_{\Lambda}$ and eigenvectors $u^{I;NZ}_{K\beta\gamma;\Lambda}$ of the norm overlap:

$$\sum_{K'\beta'\gamma'}\mathcal{N}^{I;NZ}_{K\beta\gamma K'\beta'\gamma'}u^{I;NZ}_{K'\beta'\gamma';\Lambda} = n^{I;NZ}_{\Lambda}u^{I;NZ}_{K\beta\gamma;\Lambda}. \quad (16)$$

This orthonormal basis is known as the natural basis and for $n_\Lambda^{I;NZ}$ values such that $n_\Lambda^{I;NZ}/n_{max}^{I,NZ} > \zeta$, the natural states are defined by

$$|\Lambda^{IM;NZ}\rangle = \sum_{K\beta\gamma} \frac{u_{K\beta\gamma;\Lambda}^{I;NZ}}{\sqrt{n_\Lambda^{I;NZ}}} |IMK;NZ;\beta\gamma\rangle. \quad (17)$$

Obviously, a cutoff $\zeta$ in the value of the norm eigenvalues has to be introduced to avoid linear dependencies [48]. Then, the HWG equation is transformed into a normal eigenvalue problem:

$$\sum_{\Lambda'} \langle \Lambda^{I;NZ}|\hat{H}|\Lambda'^{I;NZ}\rangle G_{\Lambda'}^{I;NZ;\sigma} = E^{I;NZ;\sigma} G_\Lambda^{I;NZ;\sigma}. \quad (18)$$

From the coefficients $G_\Lambda^{I;NZ;\sigma}$ we can define the so-called collective wave functions $F^{I;NZ;\sigma}(\beta,\gamma)$ that account for the probability density, normalized to 1, of finding the state $(I,\sigma)$ with given deformation parameters $(\beta,\gamma)$:

$$F^{I;NZ;\sigma}(\beta,\gamma) = \sum_{\Lambda,K} G_\Lambda^{I;NZ;\sigma} u_{K\beta\gamma;\Lambda}^{I;NZ} = \sum_K F_K^{I;NZ;\sigma}(\beta,\gamma). \quad (19)$$

We have also introduced $F_K^{I;NZ;\sigma}(\beta,\gamma)$ to account for the probability density of finding the state $(I,\sigma)$ with given values of $K$ and deformation parameters $(\beta,\gamma)$.

Furthermore, the expectation value of a generic operator $\hat{O}$ is given by

$$o^{I;NZ;\sigma} = \sum_{\Lambda;\Lambda'} \sum_{K\beta\gamma;K'\beta'\gamma'} G_\Lambda^{I;NZ;\sigma *} \frac{u_{K\beta\gamma;\Lambda}^{I;NZ*}}{\sqrt{n_\Lambda^{I;NZ}}} \langle\varpi|\hat{O}|\varpi'\rangle \times \frac{u_{K'\beta'\gamma';\Lambda'}^{I;NZ}}{\sqrt{n_{\Lambda'}^{I;NZ}}} G_{\Lambda'}^{I;NZ;\sigma}, \quad (20)$$

with $\langle\varpi|\hat{O}|\varpi'\rangle = \langle IMK;NZ;\beta\gamma|\hat{O}|IMK';NZ;\beta'\gamma'\rangle$. This expression can be generalized to account for transitions associated with the tensorial operator $\hat{T}_{12}$:

$$t(I_1\sigma_1 \to I_2\sigma_2) = \sum_{\Lambda;\Lambda'} \sum_{K\beta\gamma;K'\beta'\gamma'} G_\Lambda^{I_1;NZ;\sigma_1^*} \frac{u_{K\beta\gamma;\Lambda}^{I_1;NZ*}}{\sqrt{n_\Lambda^{I_1;NZ}}} \times \langle\varpi_1||\hat{T}_{12}||\varpi_2'\rangle \frac{u_{K'\beta'\gamma';\Lambda'}^{I_2;NZ}}{\sqrt{n_{\Lambda'}^{I_2;NZ}}} G_{\Lambda'}^{I_2;NZ;\sigma_2}, \quad (21)$$

where $\langle\varpi_1||\hat{T}_{12}||\varpi_2'\rangle = \langle I_1K;NZ;\beta\gamma||\hat{T}_{12}||I_2K';NZ;\beta'\gamma'\rangle$ stands for the reduced matrix element calculated according to the Wigner-Eckart theorem [2,55]. Detailed expressions for calculating these reduced matrix elements for $B(E2)$ transitions and spectroscopic quadrupole moments within this framework can be found elsewhere [5,47,49].

### B. Simpler approaches: particle number and angular momentum projection and the RVAMPIR approximation

The expressions given thus far constitute the most general framework that we are using for solving the nuclear many-body problem. Nevertheless, there are some limiting cases with a relevant physical meaning that can be deduced in a straightforward manner from them. The first is the PNP, which has already been discussed [Eq. (9)]. The second approach is the PNAMP of a single point in the $(\beta,\gamma)$ plane. Here, the wave function is of the form of Eq. (1) but without the mixing in the deformation parameters:

$$|IM;NZ;\nu;\beta,\gamma\rangle = \sum_K h_K^{I;NZ,\nu}(\beta\gamma)|IMK;NZ;\beta\gamma\rangle, \quad (22)$$

where the label $\nu$ stands for the $(2I+1)$ different states that can be obtained with the angular momentum projection. However, because of the time reversal and simplex symmetries imposed on the intrinsic wave functions, this number is reduced to $(I/2+1)$ and $[(I-1)/2]$ states for even and odd values of $I$, respectively. Moreover, if we furthermore have axial symmetry, only one state can be obtained and only for even values of $I$.

The coefficients $h_K^{I;NZ,\nu}(\beta\gamma)$ and the PNAMP energies $E^{I;NZ;\nu}(\beta,\gamma)$ are found by solving the simplified version of the HWG equation [see Eq. (13)]:

$$\sum_K \left(\mathcal{H}_{K\beta\gamma K'\beta\gamma}^{I;NZ} - E^{I;NZ;\nu}(\beta,\gamma)\mathcal{N}_{K\beta\gamma K'\beta\gamma}^{I;NZ}\right) h_{K'}^{I;NZ;\nu}(\beta,\gamma) = 0. \quad (23)$$

The remaining expressions used to solve the HWG equations are simplified in the same manner, that is, by removing the sum over $(\beta,\gamma)$ from the equations and evaluating only the diagonal part. In addition, the collective wave functions $F_K^{I;NZ;\nu}(\beta,\gamma)$ [Eq. (19)], which in analogy we shall call $H_K^{I;NZ;\nu}(\beta,\gamma)$, now give the spectral distribution in the $K$ space of the corresponding PNAMP state. A full variation of the HFB wave function in the VAP approach, in the spirit of VAMPIR, for the PN and the AM with large configuration spaces and the Gogny interaction is not yet feasible. However we can use an approximation to VAMPIR, which we shall call from now on RVAMPIR, in which the PN is handled in the VAP approach and the AM in a restricted VAP (RVAP) one. The RVAP approximation has been thoroughly studied in Refs. [58,59]. In the VAP method the whole Hilbert space associated with the HFB transformation is scanned in the variational procedure. In the RVAP method, however, only a restricted variational space of highly correlated wave functions is allowed in the minimization process. Monopole (pairing) and quadrupole ($\beta$ and $\gamma$) correlations are believed to be the most relevant degrees of freedom of atomic nuclei and are related to the particle number and the angular momentum symmetries, respectively. Since we are considering the PN symmetry in the VAP theory it seems reasonable in our case to consider the restricted Hilbert space to contain a whole set of quadrupole deformed wave functions $|\Phi(\beta,\gamma)\rangle$, which parametrically depend on $(\beta,\gamma)$. This procedure is justified by theoretical arguments [2] that establish that a VAP approach is needed for systems with weakly broken symmetries, like in the PN case where only a few Cooper pairs participate, but it can be approximated in case of strongly broken symmetries, such as deformation, where a large number of nucleons participate. Concerning the differences of this approximation as compared to VAMPIR it is clear [58] that if, besides considering the

quadrupole moments $\hat{Q}_{20}$ and $\hat{Q}_{22}$ in Eq. (9), we include higher multipole moments $\hat{Q}_{LM}$ to increase the variational space, our solution would get very close to the one of the genuine VAMPIR. With respect of the quality of our approach (again with respect to the full VAMPIR) we expect that in general it will be very similar and only in very soft nuclei, where higher modes (hexadecupole for example) are very relevant, differences may arise. But for very soft nuclei we have to question also the full VAMPIR since a GCM-like approach will be more appropriate. That means RVAMPIR is not as "restricted" as its name might imply.

Specifically, the basic RVAMPIR approach consists of the following steps:

(i) At each $(\beta_i, \gamma_i)$ value of a given set of points in the $(\beta, \gamma)$ plane perform the following:
  (a) Solve the VAP-PN equations [Eqs. (8) and (9)] to determine the $\beta$-$\gamma$ constrained HFB wave function $|\Phi(\beta, \gamma)\rangle$.
  (b) Carry out simultaneous particle number and angular momentum projection on the wave function $|\Phi(\beta, \gamma)\rangle$, what we have called $|IMK; NZ; \beta\gamma\rangle$ [see Eq. (2)], to form the linear combination of the state $|IM; NZ; \nu; \beta\gamma\rangle$ in Eq. (22).
  (c) Solve the HWG equation [Eq. (23)] for different angular momenta.

(ii) For each value of the angular momentum sort out the energies $E^{I;NZ;\nu}(\beta, \gamma)$ of Eq. (23) and find out the point $(\beta^I_{\min}, \gamma^I_{\min})$ providing the energy minimum $E^{I;NZ;\nu}_{\min}(\beta^I_{\min}, \gamma^I_{\min})$.

(iii) The solutions of the HWG equation at the points $(\beta^I_{\min}, \gamma^I_{\min})$ provide $I/2 + 1[(I-1)/2]$ states for even (odd) $I$ values, which allow us to build a partial spectrum and to calculate the transition probabilities among the different states or any other observable. One has to notice that all RVAMPIR states are orthogonal, those with different AM in an obvious way and those with the same AM because they are a solution of the same eigenvalue equation.

In the following sections we will give some examples of the convergence, consistency, and performance of the methods just described. All the many-body intrinsic wave functions and operators have been expanded in a Cartesian harmonic oscillator single-particle basis closed under rotations [60]. In particular, the rotation operator $\hat{R}(\Omega)$ has been evaluated following the expressions given in Ref. [61] and the Neergard method [62] has been used in the calculation of the norm overlaps to determine the correct sign of the Onishi formula [63–65]. The overlaps of a generic operator have been calculated using the generalized Wick theorem [64].

## III. AXIAL CALCULATIONS FOR $^{24}$Mg

Because of the huge computational cost of the full triaxial calculation, it is important to study first the axial case (with $K = 0$) to fix some relevant quantities. The most important ones are the region of $\beta$ deformation to be included in the calculation and the number of major oscillator shells in which the mean-field wave functions are expanded. The computational effort depends critically on these quantities and it is important to ensure the convergence of the results, at least in the axial case, to have a reasonable choice, which then later allows us to perform the full triaxial calculation.

The main advantage of considering only axial symmetric ($K = 0$) intrinsic wave functions $|\Phi(\beta, \gamma = 0^\circ, 180^\circ)\rangle \equiv |\Phi(\beta)\rangle$ is that the integration over the Euler angles $(a, c)$ can be done analytically and this fact reduces drastically the computational time. The simplified expressions of the axial GCM-PNAMP method can be found in detail in Ref. [5]. We first analyze the results obtained for the nucleus $^{24}$Mg using $N_{\text{shells}} = 7$ oscillator shells and $N_{\text{points}} = 31$ intrinsic wave functions distributed in the interval $(-1.5 \leqslant \beta \leqslant 1.5)$ with positive and negative values of $\beta$ corresponding to prolate $\gamma = 0^\circ$ and oblate $\gamma = 180^\circ$ shapes. The integration over the gauge angle $\varphi$ for the particle number projection part has been performed using the Fomenko expansion [66] whereas for the integration over the Euler angle $b$ a Gaussian-Legendre quadrature has been used. We have chosen $N_{\text{Fom}} = 9$ and $N_b = 16$ as the number of integration points for the particle number and the angular momentum parts of the projection, respectively. With these assumptions the expectation values for the $\hat{N}$, $\hat{Z}$, $\hat{N}^2$, $\hat{Z}^2$, and $\hat{I}^2$ operators differ by less than $10^{-8}$ from the corresponding eigenvalues. In Fig. 1(a) we plot the potential energy surfaces (PESs) along the $\beta$ direction for the VAP-PN and PNAMP approaches. The VAP-PN curve shows two differentiated minima separated by a barrier of $\sim$7.7 MeV, the lowest one at prolate deformation ($\beta = 0.5$) and the other one in the oblate part ($\beta = -0.2$). These minima are shifted toward larger deformations when the angular momentum projection is performed. In particular, a well-defined prolate minimum appears at $\beta = 0.6$ for $I = 0, 2, 4, 6, 8$, showing that a rotational band will develop from this intrinsic state. For the ground state the gain in correlation energy resulting from the restoration of the rotational symmetry amounts to $\sim$3.9 MeV. In the oblate part, we observe a minimum at $\beta = -0.4$ for $I = 0, 2$ whereas for higher values of the angular momentum the minimum vanishes. Here, the energy difference between the VAP-PN and the $I = 0$ oblate minima is $\sim$4.6 MeV.

The next step in the calculation is the configuration mixing of the PNAMP states. Hence, once the HWG equations are solved, we select as the final solutions those that belong to a plateau in the energy as a function of the number of states in the natural basis [Eq. (17)] and fulfill the orthonormality condition. To avoid duplications a detailed discussion on these issues is postponed to the triaxial case. The resulting GCM-PNAMP energies are also represented in Fig. 1(a), and the corresponding collective wave functions [Eq. (19)] are plotted in Fig. 1(b) for $\sigma = 1$ and in Fig. 1(c) for $\sigma = 2$ and $2^+_3$. In these figures we can see that the $\sigma = 1$ states are members of a rotational band, with most of the intensity of the collective wave functions concentrated around $\beta = 0.6$. This deformation corresponds to the location of the prolate minima of the different potential wells. The ground state $0^+_1$ also has a small mixing with the oblate minimum at $\beta = -0.5$. The situation is rather different for the $\sigma = 2$ states. The second $0^+$ state is a mixing of oblate and prolate configurations,

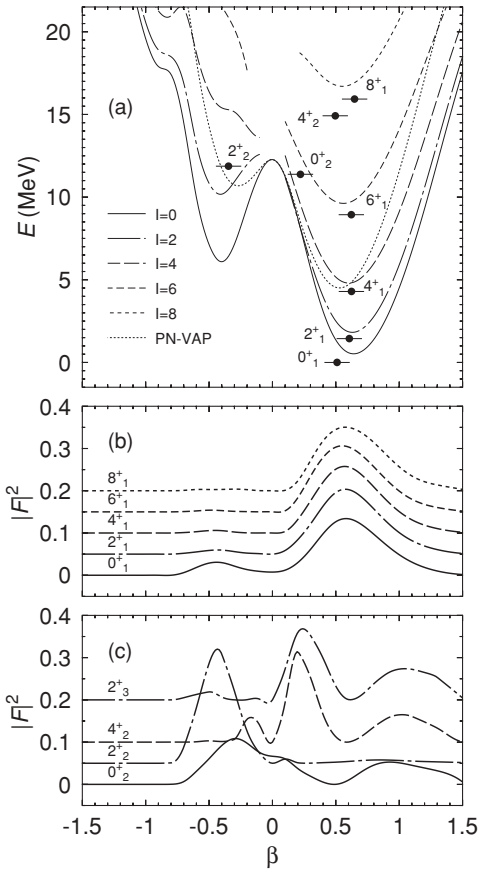


FIG. 1. (a) Potential energy surfaces along the $\beta$ deformation for particle number projection and particle number and angular momentum projection ($^{24}$Mg). The bullets correspond to the excitation energies for the different GCM levels $(I, \sigma)$ with their positions at $\bar{\beta}^{I\sigma} = \sum_\beta \beta |F^{I\sigma}(\beta)|^2$. The energy is normalized to the GCM ground-state energy ($0^+_1$). (b) Collective wave functions for the ($\sigma = 1$) GCM levels. The values of the ordinate axis are displaced by 0.05 with increasing angular momentum. (c) Same as (b) but for the ($\sigma = 2$) GCM levels and $2^+_3$ state. Positive and negative values of $\beta$ correspond to prolate ($\gamma = 0°$) and oblate ($\gamma = 180°$) shapes, respectively.

whereas the wave function of the $2^+_2$ state peaks in the oblate minimum of the corresponding PES and the $4^+_2$ state could be considered as a vibration built on the $I = 4$ prolate well with a small contribution of slightly oblate states. In the $2^+_3$ state the prolate deformations are again favored. Remembering that the purpose of this axial calculation is to determine the range of values of $\beta$ needed to obtain converged results in the low-lying energy spectrum, we observe in Figs. 1(b) and 1(c) that all the collective wave functions studied here drop to zero at the boundaries. A smaller interval, however, could not be sufficient for describing correctly the collective states. In addition, we have checked the convergence of the results as a function of the number of the points included in the GCM-PNAMP. Increasing this number to $N_{\text{points}} = 61$ still yields very similar results for the PES, GCM-PNAMP energies, and the collective wave functions as compared to the ones obtained for $N_{\text{points}} = 31$.

Finally, to test the convergence with the number of oscillator shells, we have performed a calculation with $N_{\text{shells}} = 11$ and

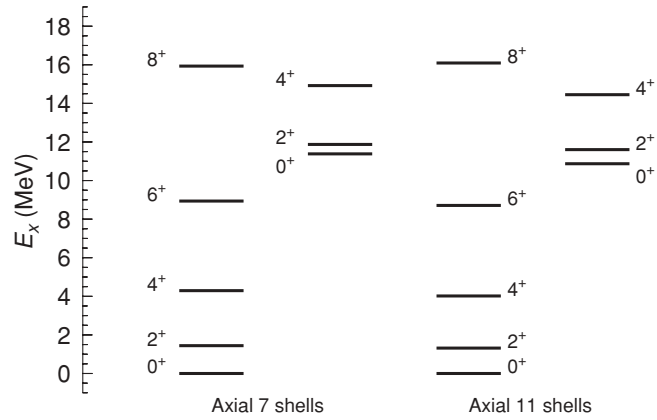


FIG. 2. Axial PNAMP-GCM excitation spectra of $^{24}$Mg obtained considering 7 shells (left) and 11 shells (right) in the calculations.

$N_{\text{points}} = 31$. It is noteworthy that, for a triaxial calculation, the computational time for $N_{\text{shells}} = 11$ is ∼30 times larger than the one used for $N_{\text{shells}} = 7$. Although this fact complicates the applicability of this method for heavy nuclei, for lighter systems the calculation with a smaller number of oscillator shells could still be sufficient. This is the case for $^{24}$Mg, where the PES and the collective wave functions calculated with $N_{\text{shells}} = 11$ (not shown) are very similar to the $N_{\text{shells}} = 7$ results. In Fig. 2 we compare the spectra obtained in the two calculations and observe a relative error of less than 10% for all the levels. Whereas the members of the $\sigma = 1$ bands almost match each other, small differences are found in the $\sigma = 2$ band. This comparison justifies that all further calculations are performed with $N_{\text{shells}} = 7$.

## IV. CONVERGENCE AND CONSISTENCY OF THE TRIAXIAL PNAMP

In this section we will study some aspects of the simultaneous particle number and angular momentum projection with triaxial shapes. First, it is important to note that the parametrization of the quadrupole deformation in terms of $(\beta, \gamma)$ variables gives a triple degeneracy in the range $0° \leqslant \gamma \leqslant 360°$ if we consider time-reversal-conserving wave functions [2]. This degeneracy corresponds to the three possible orientations of the intrinsic axis $I_3$ with respect to the $z$ axis (see Fig. 3). Therefore, the interval $0° \leqslant \gamma \leqslant 60°$ covers all the possible quadrupole deformations. However, we can take advantage of this symmetry first to improve the convergence of the integral in the Euler angles that must be carried out in the PNAMP calculation [Eq. (2)] and second to perform consistency checks of the results. We now study the convergence of the integral in the Euler angles with respect to the number of integration points in $\Omega = (a, b, c)$. We have considered the symmetries of the intrinsic wave function by reducing the integration interval to $(0 \leqslant a \leqslant \pi/2, 0 \leqslant b \leqslant \pi/2, 0 \leqslant c \leqslant \pi)$ (see Refs. [42,47,48]) and we have used Gaussian-Legendre quadratures for the numerical integration. As in the axial case, the number of integration points for the particle number projection is kept to $N_{\text{Fom}} = 9$, which is

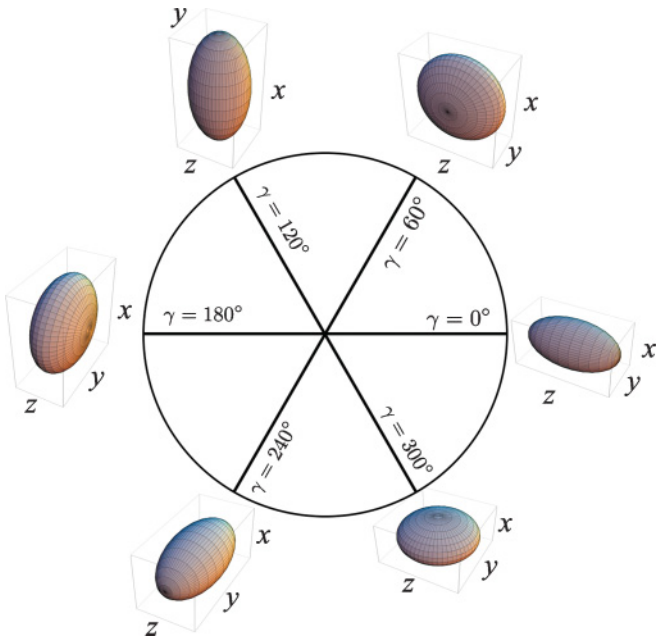


FIG. 3. (Color online) Orientations of the intrinsic deformation as a function of the $\gamma$ parameter. $\gamma = 0°, 120°, 240°$ and $\gamma = 60°, 180°, 300°$ correspond to axial symmetric prolate and oblate shapes, respectively.

sufficient to get eigenstates of the particle number operators. Naturally, the best candidate to check the convergence of the angular momentum projection is the expectation value of the total angular momentum operator $\hat{I}^2$, which, by considering Eq. (5), must be

$$\langle \hat{I}^2 \rangle_{IK} = \frac{\int \mathcal{D}^{I*}_{KK}(\Omega) \langle \Phi | \hat{I}^2 \hat{R}(\Omega) P^N P^Z | \Phi \rangle d\Omega}{\int \mathcal{D}^{I*}_{KK}(\Omega) \langle \Phi | \hat{R}(\Omega) P^N P^Z | \Phi \rangle d\Omega} = \hbar^2 I(I+1). \tag{24}$$

The convergence in the number of integration points depends on three factors, namely the orientation of the intrinsic axes, the values of $(I, K)$, and the deformation $\beta$. Let us start with the two latter factors. In Fig. 4 we plot the mean value of the total angular momentum operator as a function of $\beta$ for projected wave functions with $I = 2, 6$ and a fixed value of $\gamma = 50°$. The integration has been performed with two sets of integration points in $(a, b, c)$, $S_1 = (6, 16, 12)$ and $S_2 = (16, 16, 32)$. Here, we can observe that for the set $S_2$ the correct result of the eigenvalue is obtained for all $\beta$ and $I, K$. However, the set $S_1$ fails both for large values of $\beta$ for all $I, K$ and also for smaller deformations with high $K = 4, 6$. The poor performance of this choice is clearly seen in the latter case where substantial deviations from the correct number are observed. Therefore, as a rule of thumb, the larger the values of $(I, K)$ and $\beta$ the more integration points are needed to have good results. The final choice will be the one that is able to provide converged results for all $(I, K, \beta, \gamma)$ values. Taking into account that the symmetry axis corresponds to pure $K = 0$ states, one may assume that close to the symmetry axis only small $K$ components are present. We therefore examine the role of the orientation of the intrinsic axes in the PNAMP method. First, we explore the convergence of

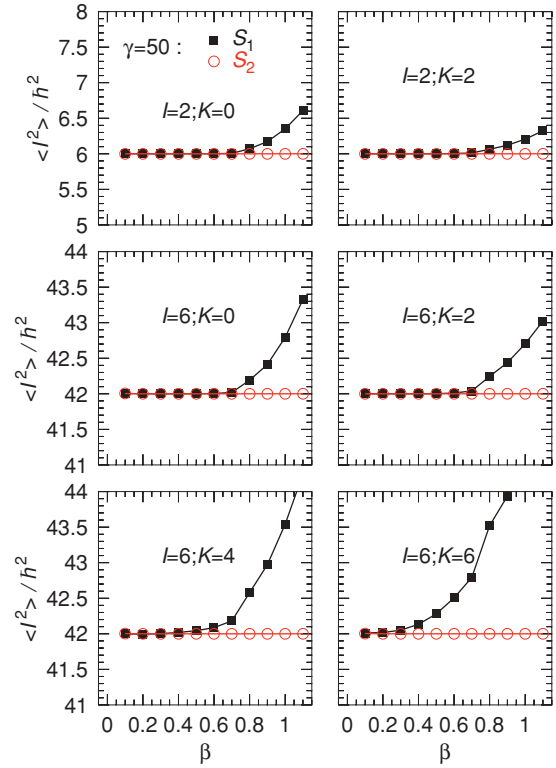


FIG. 4. (Color online) Expectation values of the total angular momentum operator calculated with angular momentum projected states $|IK\rangle$ as a function of the $\beta$ deformation ($\gamma = 50°$) and for different sets of integration points in the Euler angles $(a, b, c)$ [red circles, $S_2 = (16, 16, 32)$; black filled boxes, $S_1 = (6, 16, 12)$]. The top and bottom panels correspond to $I = 2$ and $I = 6$, and their corresponding $K$ values, respectively.

the angular momentum projection using the property given in Fig. 3 and projecting symmetric states with the same value of $\beta$ but with $\gamma' = 120° + \gamma$. If our assumption is right, we could reduce the number of integration points using instead of a given wave function an *equivalent* intrinsic wave function with an orientation closer to the $K = 0$ case. In Fig. 5 we plot as a function of $\beta$ the expectation values of the angular momentum operator for intrinsic states with $\gamma = 50°$ and also with $\gamma' = 170°$. The sets of integration points are the same as in Fig. 4. For the set $S_1$ with $\gamma = 50°$ we observe again the loss of convergence whenever $\beta$ and $I$ increase. However, very much improved results are obtained for the same set of integration points, $S_1$, but projecting the wave functions with the $\gamma = 170°$ orientation. In addition, the calculation with the set $S_2$ reveals the numerical origin of the lack of convergence for the set $S_1$ with $\gamma = 50°$. Therefore, we will use this property to define the mesh in the $(\beta, \gamma)$ plane for performing GCM-PNAMP calculations as we will see in the following.

The analysis shown in Figs. 4 and 5 has been performed with diagonal matrix elements. Since in the GCM calculations we have to consider also nondiagonal matrix elements, we have extended our study to this case. We find that to ensure a good convergence in all cases, the final set of integration points in the Euler angles has to be chosen as ($N_a = 8, N_b = 16, N_c = 16$). We can also exploit the degeneracy illustrated in

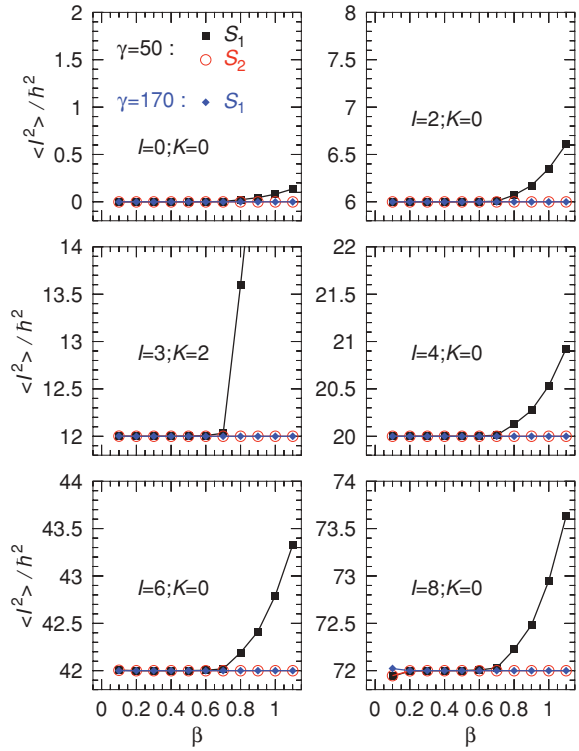


FIG. 5. (Color online) Expectation values of the total angular momentum operator between angular momentum projected states $I = 0, 2, 4, 6, 8; K = 0$ and $I = 3; K = 2$ as a function of the $\beta$ deformation and for different sets of integration points in the Euler angles and orientation of the intrinsic axes [red circles, $S_2 = (16, 16, 32)$; black filled boxes, $S_1 = (6, 16, 12)$ with $\gamma = 50°$; blue filled diamonds, $S_1 = (6, 16, 12)$ with $\gamma = 170°$].

Fig. 3 to perform a consistency test of the implementation of the PNAMP method [47]. By using symmetry properties of the point group $D_2$ it can be shown, in the notation of Eq. (2), that

$$\frac{\langle IMK; NZ; \beta\gamma = 60°|\hat{H}|IMK; NZ; \beta\gamma = 60°\rangle}{\langle IMK; NZ; \beta\gamma = 60°|IMK; NZ; \beta\gamma = 60°\rangle} = \frac{\langle I00; NZ; \beta\gamma = 180°|\hat{H}|I00; NZ; \beta\gamma = 180°\rangle}{\langle I00; NZ; \beta\gamma = 180°|I00; NZ; \beta\gamma = 180°\rangle}; \quad (25)$$

that is, the projected energy calculated with a HFB wave function with $\gamma = 60°$ is independent of $K$ and equal to the projected energy calculated with the HFB wave function with $\gamma = 180°$. A similar relation applies for the transition probabilities. In Fig. 6 we show the excitation energies and reduced transition probabilities $B(E2)$ calculated with the same oblate axially symmetric wave function ($\beta = 0.625$) but oriented differently in space with $\gamma = 60°$ (left panel) and $\gamma = 180°$ (right panel). As expected, we find that the $\gamma = 60°$ excitation spectrum and transition probabilities are independent of $K$ and therefore identical to the mixed ones. A look to the right panel corroborates also that these quantities coincide with the ones generated with the $\gamma = 180°$ intrinsic wave function. Once we have analyzed the convergence and consistency of the PNAMP method for a given point in the $(\beta, \gamma)$ plane we can study the potential energy surfaces for the

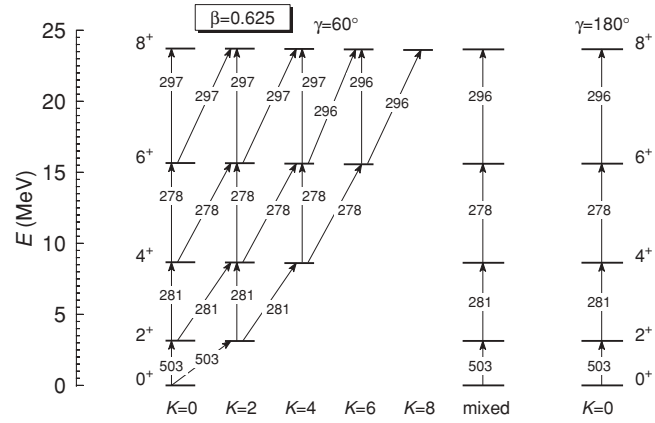


FIG. 6. (Left) Excitation energies and $B(E2)$ (in $e^2$ fm$^4$ units) values for the states before and after $K$ mixing, $|IMK\rangle$ and $|IM\rangle$, respectively, with $\beta = 0.625$ and $\gamma = 60°$. (Right) Excitation energies and $BE(2)$ values for the state $|IMK = 0\rangle$ with $\beta = 0.625$ and $\gamma = 180°$.

different approaches (VAP-PN and PNAMP with and without $K$ mixing). We explore first the role of the mesh of points needed to cover all different triaxial shapes. Given the better convergence properties for wave functions with a large $K = 0$ component (compare Fig. 5), we divide the calculation into two regions, $\gamma \in [0°, 30°]$ and $\gamma \in [150°, 180°]$ (see Fig. 7). The last interval is equivalent to $\gamma \in [30°, 60°]$ and we will transform the results to it whenever we plot the different PESs throughout this paper. Furthermore, the resolution of the PES is affected by the way we perform the discretization of the plane. In the lower panels of Fig. 7 we show the VAP-PN energy surfaces for a constant step division both in $\beta$ and $\gamma$ directions (left part) and for a division based on equilateral triangles (right part). The number of points is $N_{\text{points}} = 99$ in both cases. We observe that the distribution of the points in constant steps is not the best choice either for small $\beta$, where for many points almost degenerated states are obtained, or for large $\beta$, where a loss of resolution in $\gamma$ is observed for increasing values of $\beta$. It is precisely in this region where the interpolation between distant points produces artifacts or wrong results in the PES such as spurious oscillations, as for example in the region ($\beta \in [1.0, 1.2], \gamma \in [20°, 40°]$) or softening of the contour plots ($\beta \in [0.6, 1.1], \gamma \in [50°, 60°]$). This is rectified with a discretization based on triangles and the results presented hereafter are calculated with this mesh. Nevertheless, although only small differences around the minimum of the PES are obtained in the case of $^{24}$Mg, these effects will be enhanced for rather $\gamma$-soft and moderate $\beta$ deformed nuclei. In those cases, the division based on triangles will give much better results for the same number of total points included in the calculation and will save computing time with respect to the other mesh.

## V. TRIAXIAL CALCULATIONS FOR $^{24}$Mg

In the previous sections we have studied several aspects needed to ensure good performance of the full generator coordinate method with the particle number and triaxial angular momentum projected wave functions. This previous

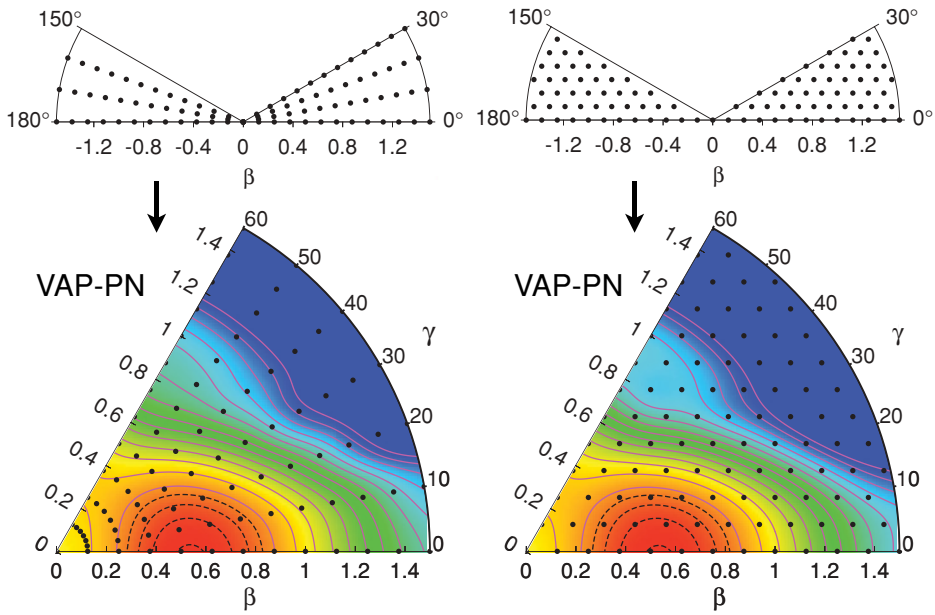


FIG. 7. (Color online) Mesh of points using constant step in $\beta$ and $\gamma$ in degrees (top left) or triangle division (top right) and the corresponding calculated VAP-PN potential energy surfaces (lower panels) transformed to the interval $\gamma \epsilon [0^\circ, 60^\circ]$. The energy is normalized to the minimum of the PES ($-196.01$ MeV) and the contour lines are divided in 1-MeV (black dashed lines) and 2-MeV steps (continuous magenta lines).

research is important because the full GCM-PNAMP calculation is very demanding of CPU time and both convergence tests and the choice of the relevant parameters should be performed in advance, but nonetheless also checked afterward. In this section the final results for $^{24}$Mg are presented; their calculation has been done with the set of integration points in the Euler angles ($N_a = 8$, $N_b = 16$, $N_c = 16$). We choose the triangular mesh with $N_{\text{points}} = 99$ shown in Fig. 7 to solve the constrained particle number projection before the variation (VAP-PN) equations. The intrinsic many-body wave functions $|\Phi(\beta, \gamma)\rangle$ are expanded in a Cartesian harmonic oscillator basis and the number of spherical shells included in this basis is $N_{\text{shells}} = 7$ with an oscillator length of $b = 1.01A^{1/6}$. In Fig. 7 the VAP-PN energy landscape is plotted, showing a single and well-defined minimum at $\beta = 0.5, \gamma = 0^\circ$ separated by $\sim$7.7 MeV from the spherical point and $\sim$6.1 MeV from the oblate saddle point at $\beta = 0.25$. These results are consistent with the ones obtained in the axial calculation (see Fig. 1) with the difference of having a saddle point in the $(\beta, \gamma)$ plane instead of a minimum on the oblate side. Similar PESs are obtained for Skyrme (HFB with PN-PAV included) [47] and relativistic (BCS without PNP) [48] interactions, although a softer surface between the spherical point and the minimum is obtained for the Skyrme interaction.

### A. Triaxial PNAMP potential energy surfaces and the RVAMPIR approach for $^{24}$Mg

The solution of the triaxial HWG equation, Eq. (13), does not require us to perform a separate angular momentum projection in the laboratory system for each component of the GCM basis states in the sense of Eq. (22). However, as in the axial case, we expect the PNAMP potential energy surfaces to provide insight and a better interpretation of the configuration mixing calculations. We can also separate the energy gain resulting from the triaxial AMP from the one from the $(\beta, \gamma)$ configuration mixing. Furthermore, they are very important because the minima of these PESs determine the associated RVAMPIR solution. The PNAMP is an involved approach that requires the solution of the HWG equation, Eq. (23), to include the $K$ mixing. The HWG eigenstates, Eq. (22), provide real eigenstates of the symmetry operators that can be used, as we shall see in the following, to generate energy spectra and to calculate transition probabilities.

In Fig. 8 we plot the normalized PNAMP energy landscapes in the $(\beta, \gamma)$ plane for the lowest eigenvalue in the $K$ space for each angular momentum $I = 0_1^+$–$8_1^+$ [see Eq. (23)]. In addition, all the points close to the spherical one, and those close to axiality for odd values of $I$, have been removed for $I \neq 0$ because their norm is very small. The first noticeable aspect is that the VAP-PN axial minimum of Fig. 7 becomes a saddle point, the minimum being displaced toward larger $\beta$ values and $\gamma > 0^\circ$ for all values of the angular momentum, although the barriers between the new minima and the axial prolate saddle points are less than 1 MeV. For $I = 0_1^+, 2_1^+$ the minima are located in $(\beta \sim 0.7, \gamma \sim 10^\circ)$ whereas with increasing value of the angular momentum we observe a softening of the PES and a displacement of the minimum to larger $\gamma$ and smaller $\beta$ deformation, $(\beta \sim 0.65, \gamma \sim 15^\circ)$ for $I = 4_1^+, 5_1^+$ and $(\beta \sim 0.55, \gamma \sim 17^\circ)$ for $I = 6_1^+, 7_1^+, 8_1^+$. We also note that in the case of odd-$I$ values the softening of the PES is in the $\gamma$ direction toward the oblate saddle point. The energy difference between the VAP-PN and the $I = 0_1^+$ minima is $\sim$4.6 MeV but the gain in energy owing to the inclusion of the triaxial degree of freedom (i.e, the difference between the triaxial minimum and the axial saddle point) is $\sim$0.7 MeV. Similar results have been reported with Skyrme and relativistic interactions although these studies of the PNAMP PES only extend to $I = 0, 2$ and the effect of increasing triaxiality with growing angular momentum has not been analyzed.

For an interpretation of the configuration mixing calculations it has become customary to plot the diagonal matrix

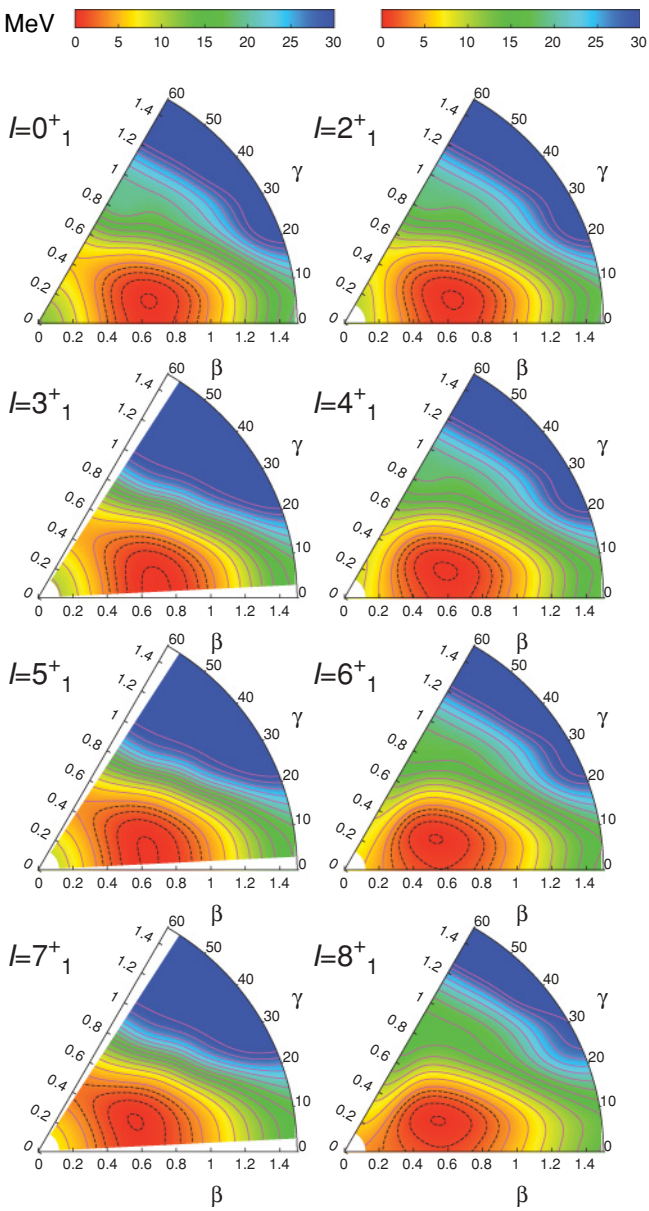


FIG. 8. (Color online) PNAMP potential energy surfaces including $K$ mixing in the $(\beta, \gamma)$ plane, with $\gamma$ in degrees, for $I = 0$–8 and the first eigenvalues in $K$ space. The PES are normalized to the minimum of the surfaces ($-200.74$, $-199.43$, $-194.04$, $-196.61$, $-190.86$, $-192.27$, $-186.09$, and $-185.33$ MeV for $I = 0$, 2, 3, 4, 5, 6, 7, and 8, respectively). The contour lines are divided in 1-MeV (black dashed lines) and 2-MeV steps (continuous magenta lines). States with projected norm less than $10^{-6}$ are removed.

elements of the normalized Hamiltonian overlap [see Eq. (14)], that is, the $IK$-projected energy

$$\mathcal{E}_K^{I;NZ}(\beta\gamma) = \frac{\mathcal{H}^{I;NZ}_{K\beta\gamma K\beta\gamma}}{\mathcal{N}^{I;NZ}_{K\beta\gamma K\beta\gamma}}, \tag{26}$$

in the $(\beta, \gamma)$ plane for the different $K$ values. Since the states $|IMK; NZ; \beta\gamma\rangle$ are not eigenstates of the angular momentum in the laboratory frame their energies do not have a physical meaning. Furthermore, the $IK$-projected energy PES and wave functions depend on the orientation of the axis in Fig. 3. To illustrate this point we present in Fig. 9 PESs calculated in three approaches for different orientations of the nucleus according to Fig. 3. We observe that, as expected, one sixth of the circle (for instance $\gamma = 0^\circ - 60^\circ$) is enough to describe the PES corresponding to the VAP-PN and the PNAMP ones (corresponding to $I = 0_1$ and $I = 2_1, 2_2$). However, for the $K$-projected PESs ($I = 2$, $K = 0$ and $I = 2$, $K = 2$) a semicircle (for instance $\gamma = 0^\circ$–$180^\circ$) is needed. Since in the laboratory system all six sectors are equivalent we explicitly see that it is the same to use the region of $\gamma = 150^\circ$–$180^\circ$ rather than $\gamma = 30^\circ$–$60^\circ$, as we have done in the GCM calculations. The contour plots in the $IK$ projection can be easily understood by looking at Fig. 3. For $I = 2$, $K = 0$, the collective AM is perpendicular to the $z$ axis and since semiclassically a rotor will prefer to rotate around the axis with the largest moment of inertia it is obvious that the energy minima are around $\gamma = 0^\circ$. For $I = 2$, $K = 2$, the collective AM is parallel to the $z$ axis and in this case the minima will be around $\gamma = 120^\circ$ and $\gamma = 240^\circ$. Especially for the latter case we see that it can be dangerous to make interpretations based on the $\gamma = 0^\circ$–$60^\circ$ sector. For nuclei with more mixing one should also care about the interpretation of the $I = 2$, $K = 0$ surface. In any case, it is important to note that the $K$ value is not a good quantum number in the laboratory frame and therefore it is not an observable. In addition, the distribution of $K$ and the corresponding PES can change depending on the orientation of the intrinsic wave function (see Fig. 3). Nevertheless, in cases where $K$ mixing is not very large this quantum number can be useful to give an interpretation of the different bands that could appear in the spectrum. As we will see in the following, $^{24}$Mg is a very good example of rather pure $|K|$ bands. One should be aware, however, that even with rather pure $|K| = 2$ bands, a mixing of $K = 2$ and $K = -2$ takes place and since these states are not orthonormal pitfalls may appear.

As discussed in Sec. II B, the minima of the PNAMP potential energy surfaces provide an approximation to an angular momentum projection in a variation after projection approach, which we have called RVAMPIR. In Table I we present the $(\beta, \gamma)$ values of the minima of the two lowest eigenstates together with the $K$ distribution of the corresponding wave functions. As we observe there is almost no mixing: The $0_1^+, 2_1^+, 4_1^+, 6_1^+, 8_1^+$ states are $K = 0$ and the $2_2^+, 3_1^+, 4_2^+, 5_1^+, 7_1^+$ states are $K = 2$. Only at the highest angular momentum do we observe very small $K$ mixing. This is not the general rule. The amount of $K$ mixing depends strongly on the nucleus and on the $(\beta, \gamma)$ point. As mentioned $^{24}$Mg seems to be a nucleus with rather small $K$ mixing. The solution of the HWG equation, Eq. (23), at the point $(\beta^I_{\min}, \gamma^I_{\min})$ provides the RVAMPIR energies and wave functions of the corresponding states. In Fig. 10 we present the energy spectrum and the calculated transition probabilities. Though we will discuss this figure in relation with the full GCM results we can compare with the axial PNAMP-GCM excitation spectrum of Fig. 2. The clear difference is the presence of a well-developed $\gamma$ band in the RVAMPIR calculations.

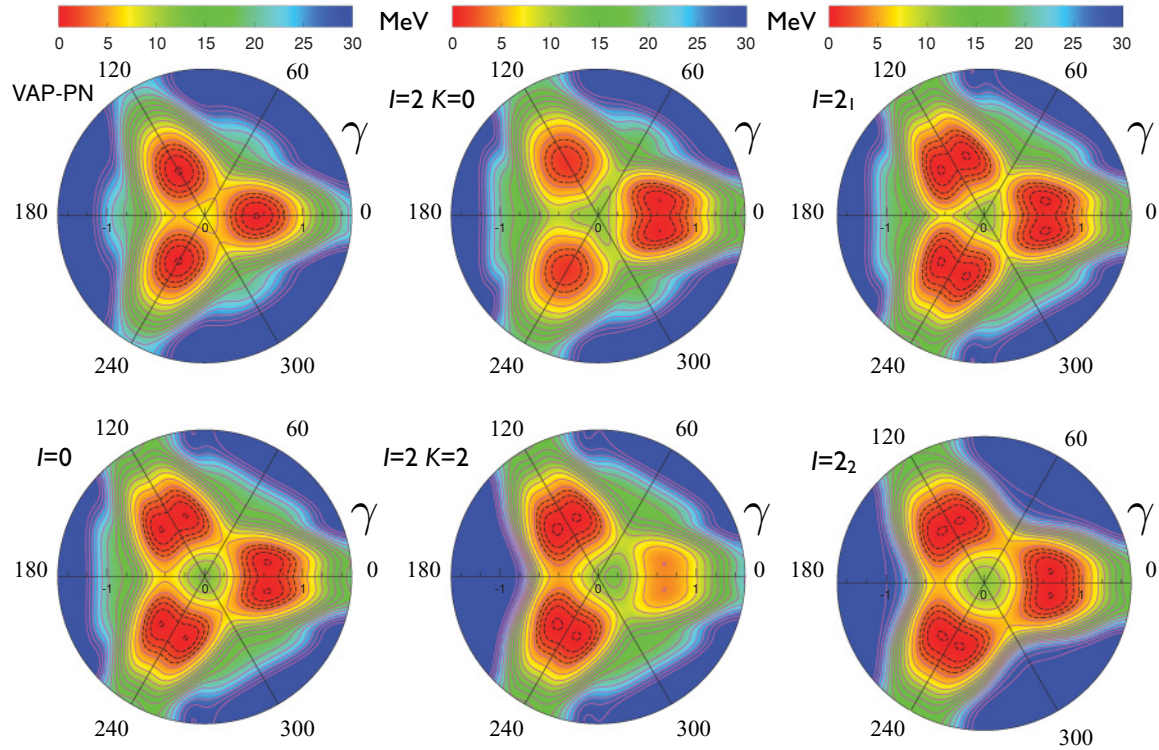


FIG. 9. (Color online) Potential energy contour plots for $^{24}$Mg in the $(\beta, \gamma)$ plane, with $\gamma$ in degrees, for $\gamma = 0°$–$360°$ in different approaches and angular momenta normalized to the corresponding minima. The contour lines are divided in 1-MeV (black dashed lines) and 2-MeV steps (continuous magenta lines). (Left panels) Top: Particle number projection (VAP), $E_{\min} = -196.02$ MeV; bottom: PNAMP approach for $I = 0\hbar$, $E_{\min} = -200.74$ MeV. (Middle panels) $IK$-projected energies according to Eq. (26). Top: $I = 2$, $K = 0$, $E_{\min} = -199.42$ MeV; bottom: $I = 2$, $K = 2$, $E_{\min} = -198.78$ MeV. (Right panels) Lowest eigenvalues of the PNAMP approach. Top: $I = 2_1$, $E_{\min} = -199.43$ MeV; bottom: $I = 2_2$, $E_{\min} = -195.18$ MeV.

### B. Configuration mixing calculations for $^{24}$Mg

The final step in the calculation of the spectrum is the GCM-PNAMP method, in which simultaneous mixing of the different deformations $(\beta, \gamma)$ and $K$ components is performed [see Eq. (1)]. As we mentioned in Sec. II A, we have to solve the HWG equations separately for each value of the angular

TABLE I. $\beta$ and $\gamma$ coordinates of the triaxial PNAMP minima after $K$ mixing as well as excitation energies and distribution of $K$ components [i.e., $|H_K^{I;NZ;\sigma}(\beta,\gamma)|^2$ see Eq. (22) and following] as a function of $I^\pi_\sigma$. The values of $(\beta, \gamma)_{\min}$ may not coincide exactly with those of Fig. 8 because of the finite size of the grid used in the calculations. The quoted values are the actual ones used in the $K$-mixing calculation. The $K = \pm 6, \pm 8$ components, not shown, are exactly zero. The highest components are printed in boldface.

| $I^+_\sigma$ | $(\beta, \gamma^\circ)_{\min}$ | $E_{\min}$ (MeV) | $K = 0$ | $K = \pm 2$ | $K = \pm 4$ |
|---|---|---|---|---|---|
| $0^+_1$ | (0.696, 8.95) | 0.000 | **1.000** | – | – |
| $2^+_1$ | (0.696, 8.95) | 1.311 | **1.000** | 0.000 | – |
| $2^+_2$ | (0.696, 8.95) | 5.556 | 0.000 | **0.500** | – |
| $3^+_1$ | (0.696, 8.95) | 6.695 | 0.000 | **0.500** | – |
| $4^+_1$ | (0.661, 19.1) | 4.129 | **1.000** | 0.000 | 0.000 |
| $4^+_2$ | (0.661, 19.1) | 8.116 | 0.000 | **0.500** | 0.000 |
| $5^+_1$ | (0.661, 19.1) | 9.883 | 0.0000 | **0.499** | 0.001 |
| $6^+_1$ | (0.545, 23.4) | 8.471 | **0.997** | 0.001 | 0.000 |
| $6^+_2$ | (0.545, 23.4) | 12.139 | 0.002 | **0.497** | 0.002 |
| $7^+_1$ | (0.545, 23.4) | 14.645 | 0.000 | **0.498** | 0.002 |
| $8^+_1$ | (0.545, 23.4) | 15.401 | **0.924** | 0.036 | 0.002 |

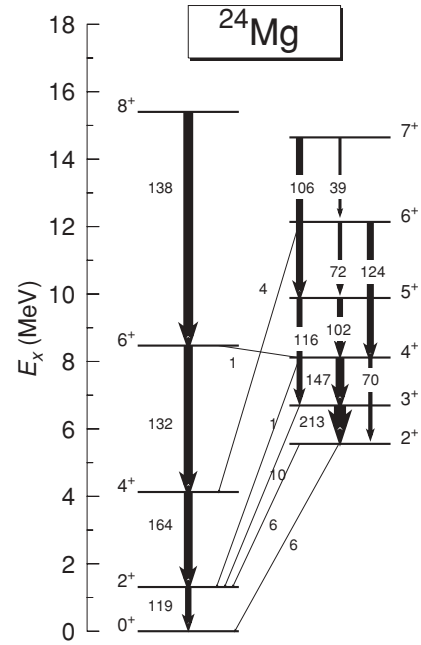


FIG. 10. RVAMPIR spectrum and transition probabilities.

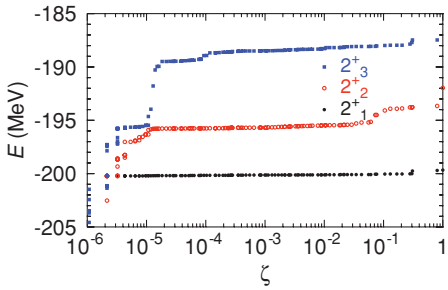


FIG. 11. (Color online) GCM-PNAMP energies ($I = 2$) as a function of the corresponding norm eigenvalue, normalized to the highest value, used as cutoff in the definition of the natural basis [Eq. (17)].

momentum. These generalized eigenvalue problems are solved by removing the linear dependence of the states with the definition of the orthonormal natural basis [Eq. (17)]. To avoid spurious states in this basis, we have to define a cutoff parameter, $\zeta$, to determine the states in the natural basis [see Eq. (17) and the text that follows it]. The convergence of the triaxial PNAMP-GCM method is showed in Fig. 11 where the lowest three energy values obtained for $I = 2$ are represented as a function of the parameter $\zeta$. Here we distinguish a region of large $\zeta$ in which the energies are decreasing followed by a range of values where the energies are nearly constant. The appearance of these plateaus is the signature of the convergence of the GCM method [67]. We observe that this plateau is better defined for the $2^+_1$ and $2^+_2$ states as compared to the $2^+_3$. Finally, for small values of $\zeta$ the linear dependence shows up and we obtain meaningless values for the energy. The final choice for $\zeta$ is a value around which we observe a wide plateau for all the levels of interest. This value must be kept constant for a given angular momentum to guarantee the orthogonality of the corresponding wave functions. This analysis has been performed for different values of the angular momentum, showing in all cases a behavior similar to the one presented in Fig. 11. Eventually, we have chosen $\zeta = 10^{-3}$ as the final value, similar to the one found in Ref. [49]. This procedure can be complemented by an inspection of the shape of the collective wave function as a function of $\zeta$.

In the central panel of Fig. 12 we now plot the spectrum of $^{24}$Mg extracted from the triaxial GCM calculations. We classify the different levels in three bands according to the corresponding $B(E2)$ values. The ground-state band is formed by a sequence of even angular momentum states with a level spacing very similar to that of a rotational band. The first excited band consists of states with $I = 2, 3, 4, 5, \ldots$ as expected for a $\gamma$ band. The third band is built of even-$I$ states on top of the second $0^+_2$ state. We can also compare the absolute value of the ground-state energy calculated with different approaches. The lowest value is obtained with the triaxial GCM-PNAMP method ($-201.36$ MeV); $-200.74$ and $-200.67$ MeV are the results for RVAMPIR and axial GCM-PNAMP approximations, respectively. Comparing the first two values we observe that the energy gained by mixing different shapes is $\approx$0.5 MeV, much less than the correlation provided by PN and/or AM restoration. However, the inclusion of the triaxial degree of freedom within the GCM framework gives a similar energy gain ($\approx$0.5 MeV) because the ground state—as well as the whole band built on top of it—is already well described by an axial calculation in this particular nucleus. Major changes, as we will see in the following, are however found for the excited bands.

Concerning the transition probabilities, we observe strong electric quadrupole intraband transitions whereas the interband $E2$ transitions are much weaker. This fact indicates different underlying structures of the bands and the absence of mixing between them. We can study the nature of these bands by

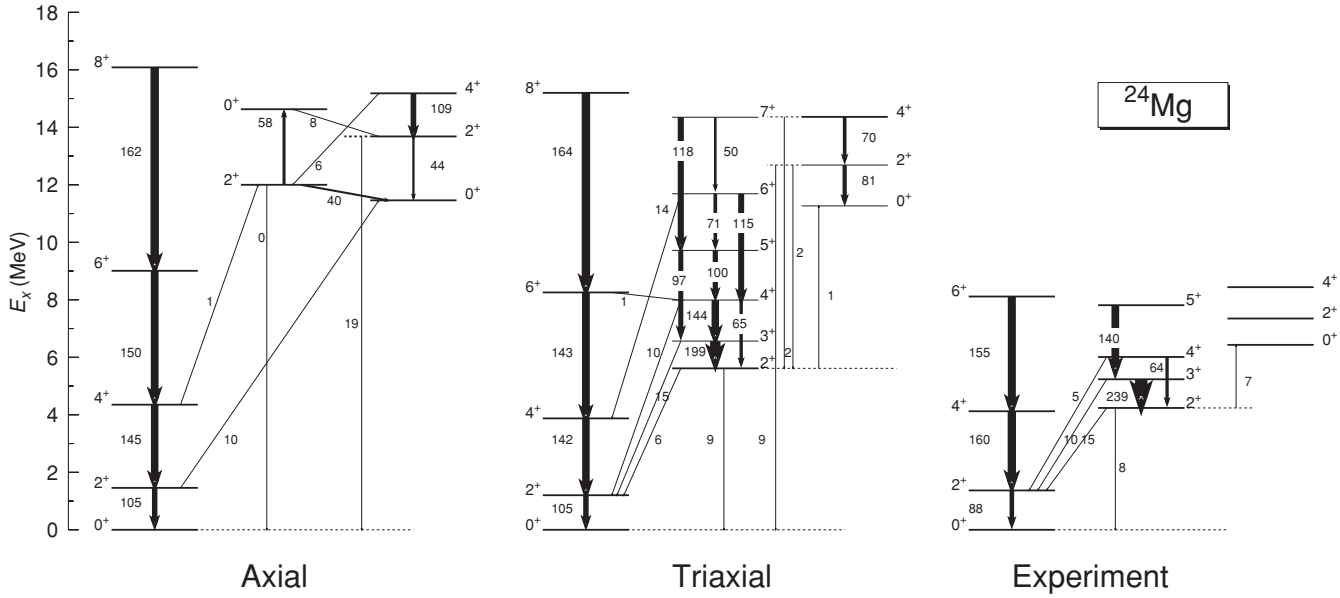


FIG. 12. Calculated excitation energies and reduced transition probabilities $B(E2)$ (in $e^2$ fm$^4$) in $^{24}$Mg obtained using axially symmetric (left) and triaxial (middle) GCM-PNAMP approaches compared to the experimental values (right). The widths of the arrows are proportional to the corresponding $B$ values. The experimental values are taken from Ref. [68].

TABLE II. Decomposition of the norm of GCM-PNAMP collective wave functions into $K$ components $[\sum_{\beta,\gamma} |F_K^{I;NZ;\sigma}(\beta,\gamma)|^2]$ for the first, second, and third bands. The highest values are printed in boldface. The excitation energies of the corresponding states are also provided.

| $I_\sigma^+$ | $E$ (MeV) | $K=0$ | $K=\pm2$ | $K=\pm4$ | $K=\pm6$ | $K=\pm8$ |
|---|---|---|---|---|---|---|
| $0_1^+$ | 0.000 | **1.000** | – | – | – | – |
| $2_1^+$ | 1.202 | **0.922** | 0.039 | – | – | – |
| $4_1^+$ | 3.875 | **0.904** | 0.016 | 0.032 | – | – |
| $6_1^+$ | 8.256 | **0.882** | 0.011 | 0.015 | 0.033 | – |
| $8_1^+$ | 15.198 | **0.834** | 0.040 | 0.017 | 0.016 | 0.010 |
| $2_2^+$ | 5.616 | 0.188 | **0.406** | – | – | – |
| $3_1^+$ | 6.564 | 0.000 | **0.500** | – | – | – |
| $4_2^+$ | 7.990 | 0.081 | **0.413** | 0.046 | – | – |
| $5_1^+$ | 9.718 | 0.000 | **0.407** | 0.093 | – | – |
| $6_2^+$ | 11.688 | 0.078 | **0.398** | 0.007 | 0.056 | – |
| $7_1^+$ | 14.349 | 0.000 | **0.379** | 0.036 | 0.085 | – |
| $0_2^+$ | 11.265 | **1.000** | – | – | – | – |
| $2_3^+$ | 12.686 | **0.958** | 0.021 | – | – | – |
| $4_3^+$ | 14.363 | **0.795** | 0.048 | 0.055 | – | – |

decomposing the collective wave functions $|F^{I;NZ;\sigma}(\beta,\gamma)|^2$ [Eq. (19)] into their $K$ components, $|F_K^{I;NZ;\sigma}(\beta,\gamma)|^2$, summing the contribution of all deformations $(\beta,\gamma)$ for each $K$. The result is shown in Table II, where we clearly observe that the first and third bands are rather pure $K=0$ whereas the second band corresponds mainly to $|K|=2$ states. Furthermore, we see that for each level the $\pm K$ components have the same values, as a direct consequence of the time-reversal conservation of the intrinsic wave functions.

The distribution of the states within these bands is supported by the values of the spectroscopic quadrupole moments:

$$Q(I\sigma)=\sqrt{\frac{16\pi}{5}}\begin{pmatrix} I & I & I \\ I & 0 & -I\end{pmatrix}\langle I;NZ\sigma||\hat{M}_2^{\rm elec}||I;NZ\sigma\rangle, \tag{27}$$

where $\hat{M}_{2\mu}^{\rm elec}=er^2Y_{2\mu}(\theta,\phi)$ are the electrical quadrupole moment operators. In the collective rotational model the spectroscopic quadrupole moments for a given $|K|$ band take the simple form [2]

$$Q_{\rm coll}(I,K)=Q_0\frac{3K^2-I(I+1)}{(I+1)(2I+3)}, \tag{28}$$

with $Q_0$ a constant deformation of the intrinsic macroscopic state. In Fig. 13 we compare the triaxial results with the values given for the collective rotational model with $K=0$ and $K=2$, normalized to $I=2$. Here we can clearly observe that the ground-state band corresponds to a rotational band $(K=0)$ whereas the second band matches a $\gamma$ band $(K=2)$ and the third band cannot be described in this simple picture.

We also plot the probability distribution $|F^{I;NZ;\sigma}(\beta,\gamma)|^2$ of each GCM state in the $(\beta,\gamma)$ surface (Fig. 14) by summing all the possible $K$ components. The most noticeable aspect is that all the states belonging to the same band have a very similar probability distribution in the $(\beta,\gamma)$ plane and

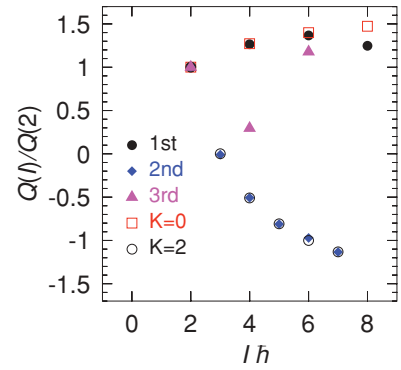


FIG. 13. (Color online) Spectroscopic quadrupole moments as a function of the angular momentum $I$ calculated for the states in the first (black bullets), second (blue diamonds), and third (magenta triangles) bands and for the vibrational-rotational collective model with $K=0$ (red boxes) and $K=2$ (black circles).

that the overlap between states of different bands is small. One could assume that these facts will lead to the intraband and interband $B(E2)$ values shown in Fig. 12. However, as we shall see in the following, the reason for the small interband transitions seems to be more related to a $K$-hindrance aspect based on the fact that the ground band is a pure $K=0$ and the $\gamma$ band a rather pure $|K|=2$ band. In

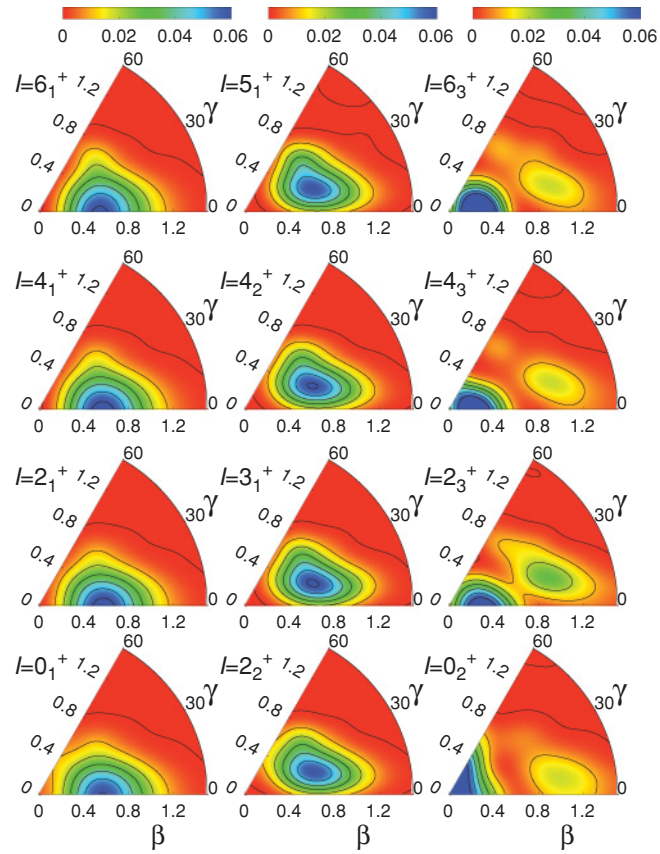


FIG. 14. (Color online) GCM-PNAMP collective wave functions $|F^{I;NZ;\sigma}(\beta,\gamma)|^2$ in the $(\beta,\gamma)$ plane, with $\gamma$ in degrees, for the ground-state (left), second (middle), and third (right) bands, respectively. Contour lines are separated in 0.01 units.

particular, all the states in the first band have a well-defined maximum at ($\beta \sim 0.58, \gamma = 0^\circ$) and the probability drops rather symmetrically in the $\beta$ and $\gamma$ directions. For the second band, the probability distribution is concentrated in a region of the plane with ($\beta \in [0.4 - 1.0], \gamma \in [0^\circ, 35^\circ]$) with maxima around ($\beta \sim 0.7, \gamma \sim 18^\circ$). Finally, the states belonging to the third band show a high probability of having spherical shape ($0_2^+$) or being slightly prolate ($2_3^+, 4_3^+, 6_3^+$) combined with a non-negligible mixing of strongly deformed states in the range of $\beta \in [0.8, 1.3], \gamma \in [0^\circ, 30^\circ]$. The PNAMP PES of Fig. 8 can help us to understand the probability distribution of the HWG equation. Looking at the ground band panels ($0_1^+, 2_1^+, 4_1^+, 6_1^+, 8_1^+$) of Fig. 8 we find that all show soft triaxial minima close to the axial axis, the contour lines being elongated along the radial direction and rather steep along the $\gamma$ angle. These states will mix with the mirrored ones at $\gamma = 0^\circ$ (see Fig. 9) and as a result distributions with a peak at $\gamma = 0^\circ$ similar to the ones in the left panels of Fig. 14 are expected. If we now concentrate on the panels ($3_1^+, 5_1^+, 7_1^+$), representative of the $\gamma$ band, we observe contour lines centered around a soft slightly triaxial minimum. These contours, at variance with the ones of the ground band, are softer in the $\gamma$ angle. We found that the members of the $\gamma$ band are rather pure $K = 2$ states, which means that the norms of the states along the symmetry axis ($\gamma = 0$) are zero. This axis acts as a barrier between the states above $\gamma = 0^\circ$ and the mirrored ones hindering the mechanism described for the ground band. As a result distributions similar to the ones in the middle panels of Fig. 14 will be obtained.

In Fig. 12 we have also compared the triaxial results with axial calculations. To better understand the results of this comparison, we investigate first the relationship between the axial and triaxial collective wave functions. The axial states emerge from the $\gamma = 0^\circ$–$180^\circ$ path of the $K = 0$ component of the corresponding triaxial states. In particular, we can relate the ground-state bands in both approaches and also the axial $0_2^+, 2_3^+, 4_2^+$ with the triaxial $0_2^+, 2_3^+, 4_3^+$ states (see Figs. 1 and 14). Hence, the comparison between the triaxial and axial calculations reveals that both the energies and reduced transition probabilities of the ground-state band are very similar in both cases, as expected. Nevertheless, the small $K$ mixing for $I \neq 0$ lowers the excitation energies of higher angular momentum and, therefore, the triaxial ground-state band is slightly compressed with respect to the axial band. This effect, although small, helps to improve the description of the moments of inertia within the GCM-PNAMP framework. Larger differences between the axial and triaxial calculations appear for the second and third bands. Obviously, the axial calculations are unable to describe the $\gamma$ band; but also the energies and $B(E2)$ for the third triaxial band ($K = 0$ mainly) are modified with respect to the corresponding ones in the axial case. This difference is due to both the small $K$ mixing and the triaxial configuration around $\beta \sim 1.0$ that appears already for $I = 0$ (see Fig. 14). In Table III we present the average intrinsic deformation parameters and the spectroscopic quadrupole moments obtained for the axial and triaxial calculations. In general the average $\beta$ deformation is larger in the triaxial calculations than in the axial ones. The largest differences correspond, obviously, to the states that comprise the $\gamma$ band in the triaxial case and to the $0_2^+$ state owing to the fake minimum on the oblate side of Fig. 1. Also interesting to notice is that though the most probable $\gamma$ value in the first band is zero, the average $\gamma$ values are around 15°. Also the average $\gamma$ values for the $\gamma$ band are larger than the most probable ones. For completeness we also include the values of the spectroscopic quadrupole moments.

TABLE III. Average intrinsic deformation parameters and spectroscopic quadrupole moments (in $e$ fm$^2$) in the triaxial and axial approximations.

| $I$ | $\sigma$ | $\bar{\beta}_{\rm tr}$ | $\bar{\gamma}_{\rm tr}^\circ$ | $Q_{\rm tr}^{\rm spec}$ | $\bar{\beta}_{\rm ax}$ | $\gamma_{\rm ax}^\circ$ | $Q_{\rm ax}^{\rm spec}$ |
|---|---|---|---|---|---|---|---|
| 0 | 1 | 0.644 | 14.81 | 0.00 | 0.510 | 0 | 0.00 |
| 0 | 2 | 0.515 | 25.98 | 0.00 | 0.221 | 0 | 0.00 |
| 2 | 1 | 0.658 | 13.58 | −20.80 | 0.606 | 0 | −19.94 |
| 2 | 2 | 0.709 | 23.16 | 21.59 | 0.346 | 60 | 12.70 |
| 2 | 3 | 0.642 | 16.02 | −19.66 | 0.451 | 0 | −19.33 |
| 3 | 1 | 0.717 | 22.05 | −0.18 | – | – | – |
| 4 | 1 | 0.661 | 13.65 | −26.33 | 0.623 | 0 | −25.04 |
| 4 | 2 | 0.714 | 22.60 | −10.96 | 0.495 | 0 | −20.33 |
| 4 | 3 | 0.541 | 19.95 | −18.51 | – | – | – |
| 5 | 1 | 0.720 | 22.67 | −17.51 | – | – | – |
| 6 | 1 | 0.657 | 14.51 | −28.42 | 0.622 | 0 | −26.52 |
| 6 | 2 | 0.702 | 22.92 | −20.97 | – | – | −18.08 |
| 6 | 3 | 0.535 | 17.24 | −23.16 | – | – | – |
| 7 | 1 | 0.730 | 24.07 | −24.49 | – | – | – |
| 8 | 1 | 0.701 | 15.36 | −25.96 | 0.648 | 0 | −28.18 |

At this point we would like to discuss the bands obtained in the RVAMPIR approach and plotted in Fig. 10. At first glance both bands look similar to the corresponding ones of the full GCM calculations. A more careful analysis shows that the GCM bands are slightly more compressed than the RVAMPIR ones, in better agreement with the experimental results. The transition probabilities are also very similar in both approaches. It is really surprising that the RVAMPIR is able to provide spectra and transition probabilities comparable to the full GCM approach. There are several reasons that explain this behavior. A look to Fig. 14 shows that all states of the first and second band, respectively, do have a similar probability distribution consisting of one maximum—practically at the same ($\beta, \gamma$) point for all $I$ values—and a homogeneous spread around this point. Such distributions can be very well approximated by a $\delta$ function at the given point. Furthermore, since there is no $K$ mixing either in the GCM or in the RVAMPIR there is no chance that the two approaches can differ in this respect. The maxima of band 2 are located practically at the same ($\beta, \gamma$) point in both approaches whereas for band 1 the GCM maximum appears closer to the symmetry axis. However, since the surfaces are rather flat around these points this does not matter too much. With respect to the $B(E2)$ transition probabilities we observe that they are rather similar to the ones of the GCM calculations (i.e., they are large for intraband and small for interband transitions). Interestingly, the $2_1^+$, the $2_2^+$, and the $3_1^+$ RVAMPIR states do have the same deformation parameters (see Table I; that is, we cannot argue, as in the GCM case, that the small interband transition probabilities are due to the poor overlap of the corresponding wave functions. The reason is that the ground band is a pure

$K = 0$ and the $\gamma$ band a pure $|K| = 2$ band. In fact, in this case, if we look at Eq. (21), we observe that if the factors sandwiched between the collective wave functions do not strongly mix the $K$ quantum number, then the transition probabilities are very small.

Finally, we compare the triaxial results with the available experimental data for $^{24}$Mg (see Fig. 12). We find a remarkable qualitative agreement between theory and experiment in both energies and reduced transition probabilities. In both cases we observe a rotational ground-state band, a second band associated with a $\gamma$ band, and a third band with $\Delta I = 2$. In fact, the theoretical description of the experimentally observed $\gamma$ band is one of the major achievements of the present model compared to previous implementations. Furthermore, in the particular case of $^{24}$Mg, the excitation energies within the ground band are very well described even quantitatively with the present calculations, as we see in Fig. 12. In addition, it is important to emphasize the quality of the theoretical results for the intraband and interband reduced transition probabilities, which reflect the small $K$ mixing between the corresponding bands. Although the improvement of the results with respect to the axial case is evident, the bandheads of the $\gamma$ and, especially, the third band are still calculated too high in excitation energy. This is probably due to the lack of the correlations associated with the angular momentum restoration before the variation and time-reversal symmetry breaking that are not included in this calculation. Additionally, the inclusion of two-quasiparticle states would further lower the excitation energies for these bandheads. These effects could also be present in the ground-state bands. However, all these potential improvements are beyond the scope of the present work. They would probably lead to a better quantitative description of the experimental results, although we do not expect qualitative changes in the general picture. Research in this direction is in progress.

## VI. SUMMARY

In summary, we have presented the first implementation of the GCM-PNAMP method with fully triaxial intrinsic wave functions found by solving the VAP-PN equations with the Gogny interaction. Furthermore, owing to the huge computational effort demanded by this type of calculation, we have established a protocol for good performance of the method, namely:

(i) Perform first a GCM-PNAMP with only axial $K = 0$ wave functions to choose the number of oscillator shells, the relevant interval of $\beta$ deformation, and the density of points in the collective variable.

(ii) Study the convergence of the triaxial angular momentum projection with the number of integration points in the Euler angles by looking at the expectation value of $\hat{I}^2$ in the $(\beta, \gamma)$ plane and exploit the symmetries of the intrinsic states.

(iii) Choose a triangular mesh in the $(\beta, \gamma)$ plane to avoid both redundancy near the spherical shape and spurious effects resulting from a loss of resolution for increasing $\beta$.

(iv) Select the converged states as the ones whose energy belongs to a plateau and ensure the orthogonality with the other states with the same angular momentum.

(v) Check the convergence of the results in the full triaxial calculation.

The method has been applied to the study of $^{24}$Mg, which has been chosen as a test case in previous studies with different interactions. The comparison between axial and triaxial results shows minor changes in the ground-state band, which is predicted to be an axial rotational band with $K = 0$. Only for angular momentum $I \geqslant 4$ is some $K$ mixing observed, giving rise to a small level compression. This result supports the use of axial calculations in these cases. However, the triaxial calculation is also able to reproduce the second band associated with a $\gamma$ band ($K = 2$) observed experimentally.

We have also introduced the RVAMPIR method, which provides a more affordable alternative to the full GCM procedure for the calculation of ground and $\gamma$ bands. We find that this approach provides a good description of the energy levels and the intraband and interband transition probabilities for the nucleus $^{24}$Mg.

Furthermore, the agreement between the theoretical and experimental results is in general good although some improvements beyond the scope of this work must be performed to give a better quantitative description. Some work is in progress to take into account these effects. In any case, $^{24}$Mg is not a very good example for studying strong triaxial effects like the ones mentioned in the introduction and the method will be applied in the near future to other systems where both triaxiality and $K$ mixing play a crucial role in describing the experimental data.

## ACKNOWLEDGMENTS

The authors acknowledge financial support from the Spanish Ministerio de Educación y Ciencia under Contract Nos. FPA2007-66069 and FPA2009-13377-C02-01, by the Spanish Consolider-Ingenio 2010 Programme CPAN (CSD2007-00042), and within the Programa de Ayudas para Estancias de Movilidad Posdoctoral 2008 (T.R.R).

[1] M. Bender, P.-H. Heenen, and P.-G. Reinhard, Rev. Mod. Phys. **75**, 121 (2003).

[2] P. Ring and P. Schuck, *The Nuclear Many Body Problem* (Springer-Verlag, Heidelberg, 1980).

[3] T. R. Rodríguez and J. L. Egido, Phys. Rev. Lett. **99**, 062501 (2007).

[4] T. Nikšić, D. Vretenar, and P. Ring, Phys. Rev. C **74**, 064309 (2006).

[5] R. Rodriguez-Guzman, J. L. Egido, and L. M. Robledo, Nucl. Phys. A **709**, 201 (2002).

[6] W. Schwerdtfeger *et al.*, Phys. Rev. Lett. **103**, 012501 (2009).

[7] T. R. Rodriguez, J. L. Egido, and A. Jungclaus, Phys. Lett. B **668**, 410 (2008).
[8] M. Bender, P. Bonche, and P.-H. Heenen, Phys. Rev. C **74**, 024312 (2006).
[9] T. Duguet, M. Bender, P. Bonche, and P.-H. Heenen, Phys. Lett. B **559**, 201 (2003).
[10] R. R. Rodríguez-Guzmán, J. L. Egido, and L. M. Robledo, Phys. Rev. C **69**, 054319 (2004).
[11] T. Nikšić, D. Vretenar, G. A. Lalazissis, and P. Ring, Phys. Rev. Lett. **99**, 092502 (2007).
[12] T. R. Rodriguez and J. L. Egido, Phys. Lett. B **663**, 49 (2008).
[13] R. F. Casten and P. von Brentano, Phys. Lett. B **152**, 22 (1985).
[14] E. S. Paul, D. B. Fossan, Y. Liang, R. Ma, and N. Xu, Phys. Rev. C **40**, 1255 (1989).
[15] R. F. Casten and N. V. Zamfir, Phys. Rev. Lett. **85**, 3584 (2000).
[16] P. H. Regan *et al.*, Phys. Rev. Lett. **90**, 152502 (2003).
[17] N. Itagaki, S. Hirose, T. Otsuka, S. Okabe, and K. Ikeda, Phys. Rev. C **65**, 044302 (2002).
[18] E. Clément *et al.*, Phys. Rev. C **75**, 054313 (2007).
[19] A. Obertelli *et al.*, Phys. Rev. C **80**, 031304(R) (2009).
[20] A. G. Smith *et al.*, Phys. Rev. Lett. **77**, 1711 (1996).
[21] A. Baran, K. Pomorski, A. Lukasiak, and A. Sobiczewski, Nucl. Phys. A **361**, 83 (1981).
[22] M. Bender, K. Rutz, P.-G. Reinhard, J. A. Maruhn, and W. Greiner, Phys. Rev. C **58**, 2126 (1998).
[23] M. Warda, J. L. Egido, L. M. Robledo, and K. Pomorski, Phys. Rev. C **66**, 014310 (2002).
[24] S. Ćwiok, P.-H. Heenen, and W. Nazarewicz, Nature (London) **433**, 705 (2005).
[25] P. Möller, R. Bengtsson, B. G. Carlsson, P. Olivius, and T. Ichikawa, Phys. Rev. Lett. **97**, 162502 (2006).
[26] W. Nazarewicz, J. Dudek, R. Bengtsson, T. Bengtsson, and I. Ragnarsson, Nucl. Phys. A **435**, 397 (1985).
[27] B. G. Carlsson, I. Ragnarsson, R. Bengtsson, E. O. Lieder, R. M. Lieder, and A. A. Pasternak, Phys. Rev. C **78**, 034316 (2008).
[28] R. B. Yadav *et al.*, Phys. Rev. C **78**, 044316 (2008).
[29] P. Chowdhury *et al.*, Nucl. Phys. A **485**, 136 (1988).
[30] V. Modamio *et al.*, Phys. Rev. C **79**, 024310 (2009).
[31] R. Kumar *et al.*, Phys. Rev. C **80**, 054319 (2009).
[32] S. W. Ødegård *et al.*, Phys. Rev. Lett. **86**, 5866 (2001).
[33] C. Vaman, D. B. Fossan, T. Koike, K. Starosta, I. Y. Lee, and A. O. Macchiavelli, Phys. Rev. Lett. **92**, 032501 (2004).
[34] E. Grodner *et al.*, Phys. Rev. Lett. **97**, 172501 (2006).
[35] M. Baranger and K. Kumar, Nucl. Phys. A **122**, 241 (1968).
[36] O. Castaños, A. Frank, and P. Van Isacker, Phys. Rev. Lett. **52**, 263 (1984).
[37] M. Girod and B. Grammaticos, Phys. Rev. C **27**, 2317 (1983).
[38] M. Girod, J.-P. Delaroche, A. Görgen, and A. Obertelli, Phys. Lett. B **676**, 39 (2009).
[39] L. Gaudefroy, A. Obertelli, S. Péru, N. Pillet, S. Hilaire, J.-P. Delaroche, M. Girod, and J. Libert, Phys. Rev. C **80**, 064313 (2009).
[40] T. Nikšić, Z. P. Li, D. Vretenar, L. Próchniak, J. Meng, and P. Ring, Phys. Rev. C **79**, 034303 (2009).
[41] A. Hayashi, K. Hara, and P. Ring, Phys. Rev. Lett. **53**, 337 (1984).
[42] K. Enami, K. Tanabe, and N. Yoshinaga, Phys. Rev. C **59**, 135 (1999).
[43] D. Baye and P.-H. Heenen, Phys. Rev. C **29**, 1056 (1984).
[44] H. Zduńczuk, W. Satuła, J. Dobaczewski, and M. Kosmulski, Phys. Rev. C **76**, 044304 (2007).
[45] K. W. Schmid and F. Grümmer, Rep. Prog. Phys. **50**, 731 (1987).
[46] K. W. Schmid, Prog. Part. Nucl. Phys. **52**, 565 (2004).
[47] M. Bender and P.-H. Heenen, Phys. Rev. C **78**, 024309 (2008).
[48] J. M. Yao, J. Meng, P. Ring, and D. Pena Arteaga, Phys. Rev. C **79**, 044312 (2009).
[49] J. M. Yao, J. Meng, P. Ring, and D. Vretenar, Phys. Rev. C **81**, 044311 (2010).
[50] M. Anguiano, J. L. Egido, and L. M. Robledo, Phys. Lett. B **545**, 62 (2002).
[51] J. F. Berger, M. Girod, and D. Gogny, Nucl. Phys. A **428**, 23c (1984).
[52] J. L. Egido, L. M. Robledo, and R. Rodríguez-Guzman, Phys. Rev. Lett. **93**, 082502 (2004).
[53] J. L. Egido and L. M. Robledo, Phys. Rev. Lett. **85**, 1198 (2000).
[54] M. Anguiano, J. L. Egido, and L. M. Robledo, Nucl. Phys. A **696**, 467 (2001).
[55] D. A. Varshalovich, A. N. Moskalev, and V. K. Khersonskii, *Quantum Theory of Angular Momentum* (World Scientific, Singapore, 1988).
[56] M. Anguiano, J. L. Egido, and L. M. Robledo, Nucl. Phys. A **683**, 227 (2001).
[57] A. Valor, J. L. Egido, and L. M. Robledo, Phys. Lett. B **392**, 249 (1997).
[58] T. R. Rodríguez, J. L. Egido, L. M. Robledo, and R. Rodríguez-Guzmán, Phys. Rev. C **71**, 044313 (2005).
[59] N. Schunck and J. L. Egido, Phys. Rev. C **78**, 064305 (2008).
[60] J. L. Egido, L. M. Robledo, and Y. Sun, Nucl. Phys. A **560**, 253 (1993).
[61] R. G. Nazmitdinov, L. M. Robledo, P. Ring, and J. L. Egido, Nucl. Phys. A **596**, 53 (1996).
[62] K. Neergård and E. Wüst, Nucl. Phys. A **402**, 311 (1983).
[63] N. Onishi and S. Yoshida, Nucl. Phys. **80**, 367 (1966).
[64] R. Balian and E. Brezin, Nuovo Cimento **64**, 37 (1969).
[65] K. Hara and S. Iwasaki, Nucl. Phys. A **332**, 61 (1979).
[66] V. N. Fomenko, J. Phys. A **3**, 8 (1970).
[67] P. Bonche, J. Dobaczewski, H. Flocard, P.-H. Heenen, and J. Meyer, Nucl. Phys. A **510**, 466 (1990).
[68] Evaluated Nuclear Structure Data File [http://www.nndc.bnl.gov/ensdf/].